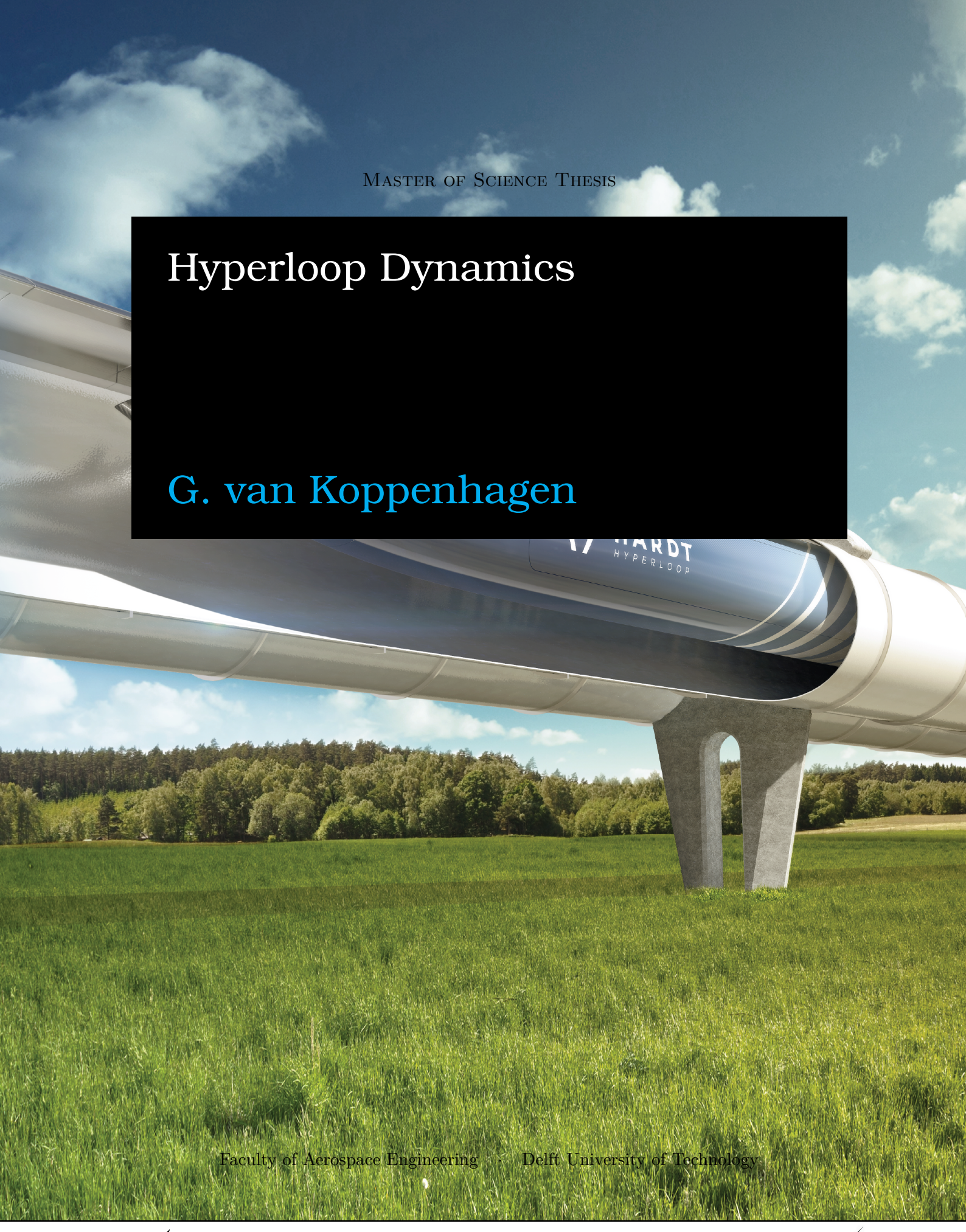

Master of Science Thesis

Hyperloop Dynamics

G. van Koppenhagen

Faculty of Aerospace Engineering · Delft University of Technology

TU Delft Delft University of Technology

Hyperloop Dynamics

Master of Science Thesis

For obtaining the degree of Master of Science in Aerospace Engineering
at Delft University of Technology

G. van Koppenhagen

08-05-2018

Faculty of Aerospace Engineering · Delft University of Technology

The work in this thesis was supported by Hardt Global Mobility. Their cooperation is gratefully acknowledged.

Delft University of Technology
Faculty of Aerospace Engineering
Department of Aerospace Structures and Materials

GRADUATION COMMITTEE

Dated: 08-05-2018

Chair holder:

Prof.dr.ir. R. Benedictus

Committee members:

Dr.ir. O.K. Bergsma

Dr.ir. E. van Kampen

Abstract

A proposed future mode of mass transit is the hyperloop system, in which magnetically levitating passenger pods travel at high speed through a tube held at low pressure. This thesis will investigate the dynamics of such a system, and determine the influence of various parameters on the dynamic response of the system. The tube has been modelled using an implicit dynamic finite element model, coupled to a vehicle model based on rigid body dynamics by a PID controlled force, which simulates the magnetic suspension. The influence of several vehicle and infrastructure parameters on the overall dynamics has been determined, and several interesting resonance and cancellation cases have been observed. The results prove the hyperloop concept is feasible from a dynamics point of view, while the methodology is readily adapted for use with more realistic vehicle models for future hyperloop design work.

Table of Contents

List of Figures

List of Tables

Chapter 1

Introduction

In 2013 Elon Musk published a white paper to introduce his vision for the future of mass transport systems. Dubbed the hyperloop, he envisioned pods floating on air bearings travelling through tubes held at near vacuum at speeds up to $1000 kmh^{-1}$ [2]. To further encourage the development of such systems, his company SpaceX organized a competition for teams from around the world to design and construct pods, and bring them to the SpaceX headquarters for a test in a test track specially build for the competition. A team from the TU Delft joined this competition, discarding the concept of air bearings as infeasible and building a pod based on magnetic levitation. After the competition, several team members founded a new company, Hardt Global Mobility, to further develop the hyperloop concept and to work on the realization of a hyperloop route in Europe.

To realize the hyperloop within Europe a greater understanding of the system as a whole is needed. This thesis will focus on the dynamic behaviour of the system. The system as currently envisioned will see pods suspended from actively controlled magnets running through a low pressure environment in a tube resting on pillars. It is expected that a form of secondary suspension will also be required to provide a comfortable ride beyond what can be achieved with only the magnetic control systems. As the pod travels through the tube, it will deflect and vibrate. These vibrations and deflections in turn excite a motion in the pod. This dynamic interaction leads to increased dynamic loading on the tube and the pod, and if the vibrations become too harsh may lead to passenger discomfort. Understanding of the coupled behaviour of the system is therefore a required step of the design process of a hyperloop system.

The work to be done consists of two parts: the creation of a model that is capable of analysing the dynamics of a hyperloop system, and an analysis of the impact on the dynamics of a hyperloop system of various parameters. The ten parameters which will be assessed are:

- Vehicle Speed
- Vehicle Mass
- Number of Axles
- Vehicle Length

- Vehicle Spring Rate
- Vehicle Damping Rate
- Controller Gains
- Guideway Support Spacing
- Guideway Stiffness
- Guideway Imperfections

The effect of varying these parameters on the dynamic behaviour of the system will be shown, and the results will be discussed. Based on the result and discussion, conclusions and recommendations for future work will be made.

Chapter 2

Methodology

The dynamic model of the hyperloop requires a model of the hyperloop pods, a model of the tube and a method for the coupling of these models. This chapter will describe these models and their underlying assumptions. It will also establish a reasonable baseline design to be used in the simulations undertaken to understand hyperloop behaviour, and determine reasonable parameter ranges to be studied. The created models will be verified against existing cases to ensure their validity and accuracy.

2.1 Preceding Work

The development of mathematical models capable of modelling these interactions started in the nineteenth century after the collapse of a railway bridge [3]. Stokes was the first to discuss the differential equations involved in the vehicle bridge interactions problem [4]. Timoshenko provided an early solution to the problem by utilizing the assumed mode method [5].

The solutions developed since then are divided in three categories: Moving force, moving mass and moving vehicle models. Of these, moving force models are the simplest models. They ignore the inertia of the vehicle and assume that the load exerted by the vehicle is equal to the static load exerted by the vehicle at all times. They are therefore unable to model the dynamic vehicle response and only provide the dynamic response of the bridge. The solution based on the assumed mode method is the most commonly used method for solving moving force problems and several solutions have been summarized by Fryba [6]. The moving force problem has also been solved using the finite element method in several studies [7] [8] [9].

For moving mass models, the inertia of the vehicle is no longer neglected, but the dynamics of the vehicle are still ignored. In a study using the assumed mode method, Akin examines the impact of the inertia on the dynamic behaviour of the bridge, noting that at high speeds the solution of the moving mass model differs up to 80% from the moving force solutions presented by Fryba [10]. Cifuentes noted the same trend after solving the moving mass problem using the finite element method, and attributed the differences to the centripetal and Coriolis forces acting on a mass moving along a curved path [11].

More recent studies have utilized full vehicle models to examine the vehicle bridge interaction problem. Several of these models, based on the assumed mode method, are presented by Fryba [6]. These methods have also been used by several authors to model maglev vehicles [12] [13] [14] [15]. Several studies used the finite element method to solve the complete vehicle, with two schools of thought for the exact set up of the model. The first partially includes the dynamics of the vehicle in the definition of the finite elements in contact with the vehicle, thereby foregoing the need to iterate to obtain the interaction force between the vehicle and the bridge [16] [17] [18]. The alternative is the completely separate integration of the vehicle and bridge equations of motion, with an iterative step to ensure the forces and displacements of the separate systems lead to a system that is in equilibrium [19] [20] [21] [22].

Studies into maglev systems such as those of Richardson, Snyder, Cai and Ren all model the magnetic component of the vehicle suspension as a linear spring, with a stiffness determined by linearising the magnetic system around the nominal operating point of the magnet. The highly non linear nature of the magnetic system means that this linearised model breaks down when the airgap varies by about $1mm$ [12] [13] [14] [15].

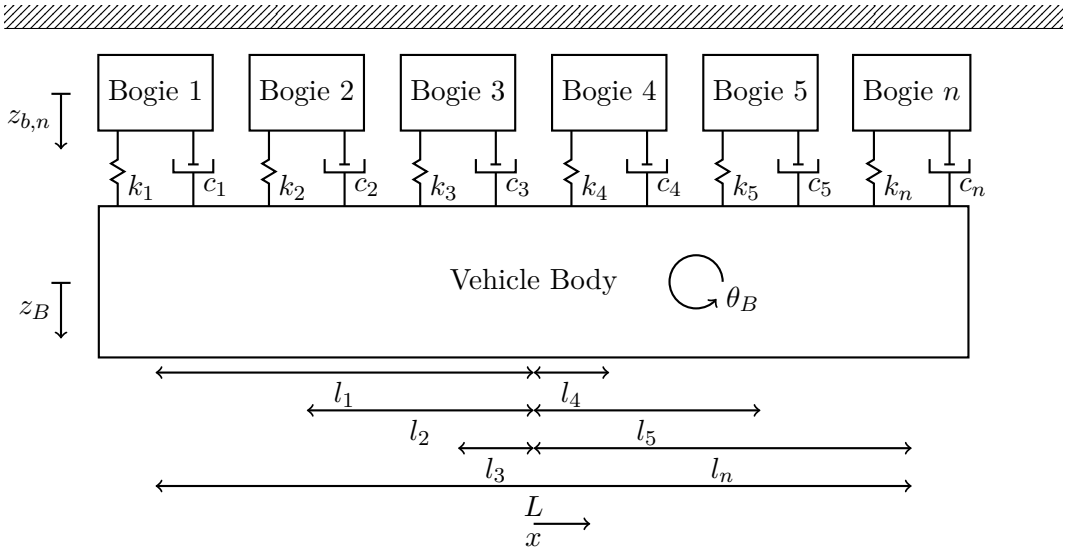

Figure 2.1: Schematic representation of a hyperloop vehicle with the degrees of freedom used in the remainder of the report.

2.2 Vehicle Model

The vehicle model is based on the current concept for the Hyperloop as envisioned by Hardt. This design concept has the passenger pods suspended from a guideway attached to the top of the tube using several dynamically controlled electromagnets.The pod will be connected to these magnets using a passive linear spring-damper system to further enhance the ride comfort of the passengers travelling in the hyperloop. A schematic representation of the vehicle is shown in figure 2.1.

Several assumptions are made to simplify the vehicle model. For the vehicle body, a rigid body model is used, neglecting the effects of deformations in the pod and bogies in the dynamic analysis. The magnets are assumed to be distributed along the length of the vehicle at a constant spacing. Pitch effects in the magnet bogies are neglected and the magnet forces are assumed to act as point loads on both the vehicle and the guideway. The mass of the pod is assumed to be distributed evenly, leading to a centre of mass in the exact centre of the pod. The centre of rotation of the pitch motion of the vehicle body is assumed to be constant and in the centre of mass of the vehicle.

Based on these assumptions, a set of parametric equations of motion can be derived describing the dynamic behaviour of the pod as it moves along the guideway. These equations are second order differential equations and are suitable for direct integration using the Newmark method [23].

2.2.1 Equations of Motion

Figure 2.2 shows the free body diagram of a single bogie. The spring and damper forces F_s and F_d acting on the bogie are a function of the relative displacement and velocity of the

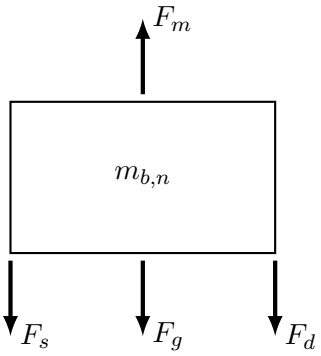

Figure 2.2: Bogie free body diagram

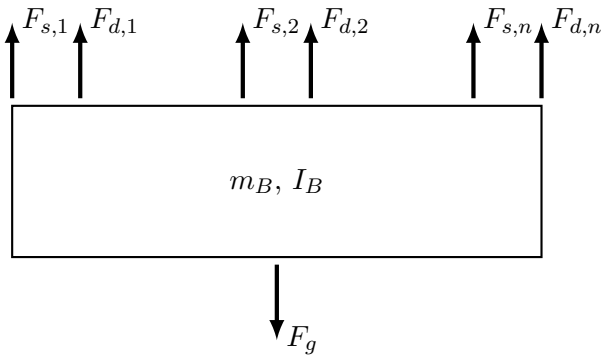

Figure 2.3: Vehicle body free body diagram

bogie and the vehicle body. For bogies not directly over the centre of mass/rotation of the body, there are additional components introduced by the body pitch motion.

Using the free body diagram in figure 2.2 and the degrees of freedom as defined in figure 2.1, a vehicle with n bogies and length L has n equations of motion governing the movement of the vehicle bogies. These equations are given in equation 2.1. They are only valid for $n \geq 2$, since the pitching motion of the vehicle is unstable if there is only a single supporting magnet.

$$m_{b,n}\ddot{z}_{b,n} + c_n(\dot{z}_{b,n} - \dot{z}_B + l_n\dot{\theta}) + k_n(z_{b,n} - z_B + l_n\theta) = F_g - F_m \tag{2.1}$$

The motion of the body has two governing equations, one for the vertical heave motion of the pod, and one for the pitching motion of the vehicle. Using the free body diagram in figure 2.3 and the same reference system as was used for the bogie equations of motion, the equations for the heave and pitch motions are equations 2.2 and 2.3 respectively.

$$m_B\ddot{z}_B + \sum_1^n (c_n(-\dot{z}_{b,n} + \dot{z}_B) + k_n(-z_{b,n} + z_B)) = F_g \tag{2.2}$$

$$-I_B\ddot{\theta}_B + \sum_1^n \left(c_n(\dot{z}_{b,n}l_n + \dot{\theta}l_n^2) + (k_n(z_{b,n}l_n + \theta l_n^2)\right) = 0 \tag{2.3}$$

Writing equations 2.1 - 2.3 in matrix form leads to equation 2.4, where $\boldsymbol{z} = [z_{b,1} \ ... \ z_{b,n} \ z_B \ \theta]^T$ and the mass, damping and stiffness matrices $\boldsymbol{M}$, $\boldsymbol{C}$ and $\boldsymbol{K}$ are given by expressions 2.5 - 2.7.

$$\boldsymbol{M_v}\ddot{\boldsymbol{z}} + \boldsymbol{C_v}\dot{\boldsymbol{z}} + \boldsymbol{K_v}\boldsymbol{z} = \boldsymbol{F_g} - \boldsymbol{F_m} \tag{2.4}$$

$$\boldsymbol{M}_v = \begin{bmatrix} m_1 & \cdots & 0 & 0 & 0 \\ \vdots & \ddots & \vdots & 0 & 0 \\ 0 & \cdots & m_n & 0 & 0 \\ 0 & \cdots & 0 & m_B & 0 \\ 0 & \cdots & 0 & 0 & -I \end{bmatrix} \tag{2.5}$$

$$\boldsymbol{C}_v = \begin{bmatrix} c_1 & \cdots & 0 & -c_1 & c_1 l_1 \\ \vdots & \ddots & \vdots & \vdots & \vdots \\ 0 & \cdots & c_n & -c_n & c_n l_n \\ -c_1 & \cdots & -c_n & \sum_1^n c_n & 0 \\ c_1 l_1 & \cdots & c_n l_n & 0 & -\sum_1^n c_n l_n^2 \end{bmatrix} \tag{2.6}$$

$$\boldsymbol{K}_v = \begin{bmatrix} k_1 & \cdots & 0 & -k_1 & k_1 l_1 \\ \vdots & \ddots & \vdots & \vdots & \vdots \\ 0 & \cdots & k_n & -k_n & k_n l_n \\ -k_1 & \cdots & -k_n & \sum_1^n k_n & 0 \\ k_1 l_1 & \cdots & k_n l_n & 0 & -\sum_1^n k_n l_n^2 \end{bmatrix} \tag{2.7}$$

2.2.2 Time Integration

Equation 2.4 is of a form readily integrated using the implicit Newmark direct integration method, a common scheme utilized by most authors referenced in section 2.1. The displacement and velocity are assumed to be of the form given in equations 2.8 and 2.9, where α and δ are integration parameters that can be used to tune the integration accuracy of stability [24]. Using $\alpha = \frac{1}{4}$ and $\delta = \frac{1}{2}$ as proposed by Newmark in his original discussion of the method, the scheme is unconditionally stable [23]. Besided equations 2.8 and 2.9, the equilibrium equation 2.4 is also considered at time $t + \Delta t$.

$$\dot{\boldsymbol{z}}^{t+\Delta t} = \dot{\boldsymbol{z}}^t + \left[(1-\delta)\ddot{\boldsymbol{z}}^t + \delta\ddot{\boldsymbol{z}}^{t+\Delta t}\right]\Delta t \tag{2.8}$$

$$\boldsymbol{z}^{t+\Delta t} = \boldsymbol{z}^t + \dot{\boldsymbol{z}}^t\Delta t + \left[\left(\frac{1}{2} - \alpha\right)\ddot{\boldsymbol{z}}^t + \alpha\ddot{\boldsymbol{z}}^{t+\Delta t}\right]\Delta t^2 \tag{2.9}$$

After some algebraic manipulation, the scheme then uses equations 2.10 -2.14 to determine the values of $\boldsymbol{U}$ and its derivatives at $t = t + \Delta t$ [24]. The scheme is started by calculating the equivalent stiffness of the system K_{eff} using equation 2.10. For every time step, the equivalent load at time $t + \Delta t$ is calculated using equation 2.11. The updated displacements

Constant	Expression
a_0	$\frac{1}{\alpha\Delta t^2}$
a_1	$\frac{\delta}{\alpha\Delta t}$
a_2	$\frac{1}{\alpha\Delta t}$
a_3	$\frac{1}{2\alpha} - 1$
a_4	$\frac{\delta}{\alpha} - 1$
a_5	$\frac{\Delta t}{2}\left(\frac{\delta}{\alpha} - 2\right)$
a_6	$\Delta t(1-\delta)$
a_7	$\delta\Delta t$

Table 2.1: Expressions to determine Newmark integration constants.

at time $t = t + \Delta t$ are calculated using equation 2.12. These displacements are in turn used to determine the derivatives of the displacement using equations 2.13 and2.14. The integration constants a_0-a_7 are determined using the expressions given in table 2.1.

$$\boldsymbol{K}_{eff} = \boldsymbol{K} + a_0\boldsymbol{M} + a_1\boldsymbol{C} \tag{2.10}$$

$$\boldsymbol{F}_{eff}^{t+\Delta t} = \boldsymbol{F}_{g}^{t+\Delta t}\boldsymbol{F}_{m}^{t+\Delta t} + \boldsymbol{M}(a_0\boldsymbol{z}^t + a_2\dot{\boldsymbol{z}}^t + a_3\ddot{\boldsymbol{z}}^t) + \boldsymbol{C}(a_1\boldsymbol{z}^t + a_4\dot{\boldsymbol{z}}^t + a_5\ddot{\boldsymbol{z}}^t) \tag{2.11}$$

$$\boldsymbol{K}_{eff}\boldsymbol{z}^{t+\Delta t} = \boldsymbol{F}_{eff}^{t+\Delta t} \tag{2.12}$$

$$\ddot{\boldsymbol{z}}^{t+\Delta t} = a_0(\boldsymbol{z}^{t+\Delta t} - \boldsymbol{z}^t) - a_2\dot{\boldsymbol{z}}^t - a_3\ddot{\boldsymbol{z}}^t \tag{2.13}$$

$$\dot{\boldsymbol{z}}^{t+\Delta t} = \dot{\boldsymbol{z}}^t + a_6\ddot{\boldsymbol{z}}^t + a_7\ddot{\boldsymbol{z}}^{t+\Delta t} \tag{2.14}$$

The equivalent load $\hat{\boldsymbol{F}}_{eff}^{t+\Delta t}$ is composed of three components as given in equation 2.11: A constant gravity load ($\boldsymbol{F}_g$) acting in the individual centres of mass of the bogies and vehicle body, an inertial load vector dependent on the accelerations, velocities and displacements at time t, and the magnetic load vector ($\boldsymbol{F}_m^{t+\Delta t}$) acting on the bogies. The method for determining $\boldsymbol{F}_m^{t+\Delta t}$ will be discussed in section 2.4

2.3 Tube Model

The tube in which a hyperloop pod will operate is currently envisioned as a long, continuous section of round tubing held under a low pressure. To determine the response of the vehicle under steady state operating conditions on a continuous discretely supported guideway, the running across several dozen spans must be determined [14]. As discussed in section 2.1, two common ways of determining the response of the guideway exist in literature: finite element analysis and the assumed mode method. For interconnected sections of tubing, where the motions of the individual spans are not independent, the complexity of the assumed mode method increases rapidly, and using the finite element method to model the tube is a more convenient solution.

2.3.1 Equations of Motion

The focus of this study is on the vertical dynamics of the tube and pod, and therefore a model consisting of 1D beam elements will suffice. The currently expected tube diameter is around four meters, while span lengths are expected to be on the order of $30 - 40m$. The beams are therefore not likely to be slender, and Timoshenko beam elements are therefore required in the analysis. At high velocities, Azimi [17] and Moghaddas [18] showed that the effects of shear deformation and rotary inertia in the formulation of the of the Timoshenko elements is required for the analysis of vehicle-bridge interactions. The mass and stiffness matrices are of a Timoshenko beam element with length L, area moment of inertia I, cross sectional area A and density ρ are given by given by equations 2.15 and 2.16 [25], with $\boldsymbol{M_t}$ and $\boldsymbol{M_r}$ as the rotational and translational mass matrices respectively.

$$\boldsymbol{M_b} = \frac{\rho AL}{210(1+\Phi)^2}\boldsymbol{M}_{b,t} + \frac{\rho I}{30(1+\Phi)^2 L}\boldsymbol{M}_{b,r}$$

$Where:$

$$\boldsymbol{M}_{b,t} = \begin{Bmatrix} (7\Phi^2+147\Phi+78) & (35\Phi^2+77\Phi+44)\frac{L}{4} & (35\Phi^2+63\Phi+27) & -(35\Phi^2+63\Phi+26)\frac{L}{4} \\ & (7\Phi^2+14\Phi+8)\frac{L^2}{4} & (35\Phi^2+63\Phi+26)\frac{L}{4} & -(7\Phi^2+14\Phi+6)\frac{L^2}{4} \\ & & (70\Phi^2+147\Phi+78) & -(35\Phi^2+77\Phi+44)\frac{L}{4} \\ Symmetric & & & (7\Phi^2+14\Phi+8)\frac{L^2}{4} \end{Bmatrix}$$

$$\boldsymbol{M}_{b,r} = \begin{Bmatrix} 36 & -(15\Phi-3)L & -36 & -(15\Phi-3)L \\ & (10\Phi^2+5\Phi+4)L^2 & (15\Phi-3)L & (5\Phi^2-5\Phi-1)L^2 \\ & & 36 & (15\Phi-3)L \\ Symmetric & & & (10\Phi^2+5\Phi+4)L^2 \end{Bmatrix} \tag{2.15}$$

$$\boldsymbol{K_b} = \frac{EI}{(1+\Phi)L^3}\begin{Bmatrix} 12 & 6L & -12 & 6L \\ & (4+\Phi)L^2 & -6L & (2-\Phi)L^2 \\ & & 12 & -6L \\ Symmetric & & & (4+\Phi)L^2 \end{Bmatrix} \tag{2.16}$$

In equations 2.15 and 2.16 the term Φ is a shear correction factor, determined by equation 2.17 [26]. The coefficient a in this equation is the relative importance of shear deformations

compared to bending deformations for a given cross section. For a thin walled circular section, the value of a has been determined by Cowper to be given by equation 2.18 [27]. For a steel tube with a Poisson ratio of $\nu = 0.3$, this leads to a shear coefficient of $a = 0.53$.

$$\Phi = \frac{24}{L^2}\left(\frac{I}{aA}\right)(1+\nu) \tag{2.17}$$

$$a = \frac{2(1+\nu)}{4+3\nu} \tag{2.18}$$

Using the mass and stiffness matrices the dynamic equation of motion of the tube can be expressed in a similar form to the vehicle equation of motion in equation 2.4, as given in equation 2.19. The matrices $\boldsymbol{K}$ and $\boldsymbol{M}$ are the global assembled matrices of the complete length of tube, and $\boldsymbol{U}$ is the vector of all degrees of freedom in the analysis. Initial runs of the model showed that a vibration introduced as the vehicle first comes into contact with the guideway would propagate through the simulated domain rather rapidly, and then reflect of the end of the domain back into the path of the vehicle. This interfered with the generated results, and Rayleigh damping of the form in equation 2.20 [24] was added to the model to damp this vibration out of the system before it reaches the vehicle. The constants μ and λ in equation 2.20 are taken as 0.1 and 0.001 respectively.

$$\boldsymbol{M_b}\ddot{\boldsymbol{U}} + \boldsymbol{C_b}\dot{\boldsymbol{U}} + \boldsymbol{K_b}\boldsymbol{U} = \boldsymbol{F_m} \tag{2.19}$$

$$\boldsymbol{C_b} = \mu\boldsymbol{M_b} + \lambda\boldsymbol{K_b} \tag{2.20}$$

2.3.2 Time Integration

The equations of motion of the tube are integrated using the Newmark method. The resulting equations are of the same form as the equations used to integrate the vehicle equations of motion described in section 2.2.2. The equivalent load vector $\boldsymbol{F}_{eff}^{t+\Delta t}$ contains an inertial load vector consisting of the same terms as those in equation 2.11 and the magnetic load vector acting on the tube. The vehicle displacement vectors $\boldsymbol{z}$ are replaced by the tube displacement vectors $\boldsymbol{U}$.

The magnetic load vector acting on the tube can be determined using the magnetic load vector acting on the vehicle $\boldsymbol{F}_m^{t+\Delta t}$. Since the vehicle is moving the individual magnetic forces need to be converted into their equivalent nodal loads using equation 2.21. Here $\boldsymbol{N}^i(x^i)$ is the vector of interpolation functions of the element upon which the force generated at the i-th bogie acts, at location x^i on the element, and $F_m^{i,\,t+\Delta t}$ is the i-th entry in the magnetic load vector $\boldsymbol{F}_m^{t+\Delta t}$. The determination of $\boldsymbol{F}_m^{t+\Delta t}$ will be handled in section 2.4. After determining $\boldsymbol{F}_m^{t+\Delta t}$ for each vehicle axle, the loads are superimposed into a single load vector corresponding to the global bridge nodes.

$$\boldsymbol{F}_m^{t+\Delta t} = F_m^{i,\,t+\Delta t}\boldsymbol{N}^i(x^i) \tag{2.21}$$

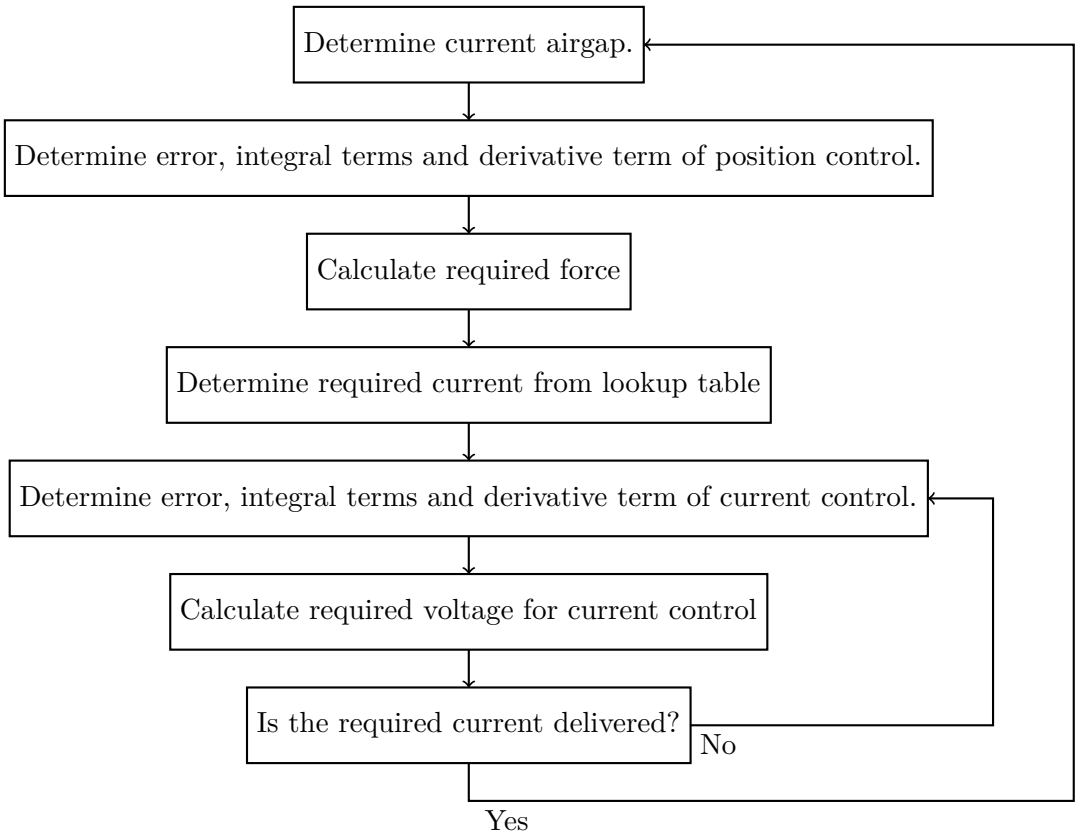

Figure 2.4: Overview of procedure for position control of magnet as implemented at Hardt. The inner control loop for current control operates at a significantly higher frequency than the position control loop.

2.4 Interaction Model

The vehicle model and the tube model described in sections 2.2 and 2.3 are linked by the magnetic force generated in the vehicle bogies. The magnets levitation system envisioned by Hardt is based around the use of permanent magnets. The primary attractive force is provided by a permanent magnet. Such a system was proven to be unstable for all configurations by Samuel Earnshaw in the late nineteenth century [28]. To overcome this, the attractive force of the permanent magnet will be attenuated using an electro-magnet.

The force generated by an electro-magnet is non-linear in terms of the air gap of the magnet and the current applied to the coils surrounding the magnet [29]. To control the position of the magnet bogie with respect to the guideway, the force generated by the magnet can be modulated by changing the current flowing through the magnet coils. Since both the dependence on air gap and on the applied current are non-linear relations it is difficult to use these non-linear relations directly in the control system. Instead, Hardt uses the control scheme shown in figure 2.4.

The scheme controls the force generated by the magnets to maintain a constant air gap. Based on the current airgap and the force required, the current in the magnets can be determined. The non-linearity in the relation between force, current and air gap is avoided by using a pre

determined look-up table of force, air gap and current values. Based on the required force and the air gap at a certain point in time, the current required can be determined. Another control loop is then used to rapidly bring the current applied to the magnet to the required value.

Simulating the magnetic and electronic components of the scheme in figure 2.4 will introduce significant complexities and unknowns into the model. The challenges of accurately modelling the magnetic system falls outside the scope of this study. By assuming that the magnetic system implemented is able to reproduce the magnetic force requested by the position controller, this step can be bypassed. This assumption rests on the ability of the magnetic system to be able to modulate the current (and thereby the force) at a significantly higher frequency than is required for stable position control.

A relatively straight forward method for position control that has wide spread adoption in control applications is Proportional-Integral-Derivative (PID) control. It was first described mathematically by Minorsky [30] for use as an automated method to keep ships on-course based on observations of helmsmen working to keep their ships on course. It uses both the absolute error in position (or whichever variable is controlled for) as well as the accumulation of error over time and the rate of change in error. Equation 2.22 is the generic form of the PID control scheme. The output variable u is governed by the error e, which is the difference between the setpoint, the desired value of some variable, and the actual value of that variable. The gains K_p, K_i and K_d can be used to tune the response of the system to errors.

$$u(t) = K_p e(t) + K_i \int_0^t e(\tau)d\tau + K_d \frac{de(t)}{dt} \tag{2.22}$$

Equation 2.22 is the continuous time version of the PID control scheme. To implement the scheme within the discrete time integration scheme described in sections 2.2 and 2.3 some modifications are needed. For each bogie, the magnetic force $F_m^{t+\Delta t}$ must be determined. The controlled variable is the error between the setpoint value for the magnetic airgap and the distance between the bogie and the guideway. The integral portion of equation 2.22 can be calculated using the trapezoidal rule, while the differential part of equation 2.22 can be evaluated using a backwards difference scheme. Using these modifications, the expression to determine $F_{m,n}^{t+\Delta t}$,the magnet force in bogie n, is given by equation 2.23. The error at time t is given by equation 2.24, where $\boldsymbol{N}_n(x_n)$ is the vector of interpolating functions of the bridge elements evaluated at the location of the bogie x_n, and $\boldsymbol{U}_{br,n}$ is the vector containing the values of the degrees of freedom of the bridge element in contact.

$$F_{m,n}^{t+\Delta t} = K_p e_n^t + K_i \sum_{t=0}^{t} \left[e_n^{t-\Delta t} dt + \frac{e_n^t - e_n^{t-\Delta t}}{2} dt \right] + K_d \frac{e_n^t - e_n^{t-\Delta t}}{dt} \tag{2.23}$$

$$e_n^t = \boldsymbol{N}_n^T(x_n)\boldsymbol{U}_{br,n} - z_n^t \tag{2.24}$$

Using equations 2.4, 2.19 and 2.23 with the integration scheme described in sections 2.2 and 2.3 the dynamic behaviour of a hyperloop vehicle running over a flexible guideway can be simulated. A schematic overview of the solution procedure is given in figure 2.5. Note that since $F_m^{t+\Delta t}$ is directly determined using equation 2.23, the iterative process used in previous methods to ensure the displacements and forces between the bridge and the vehicle are balanced can be skipped.

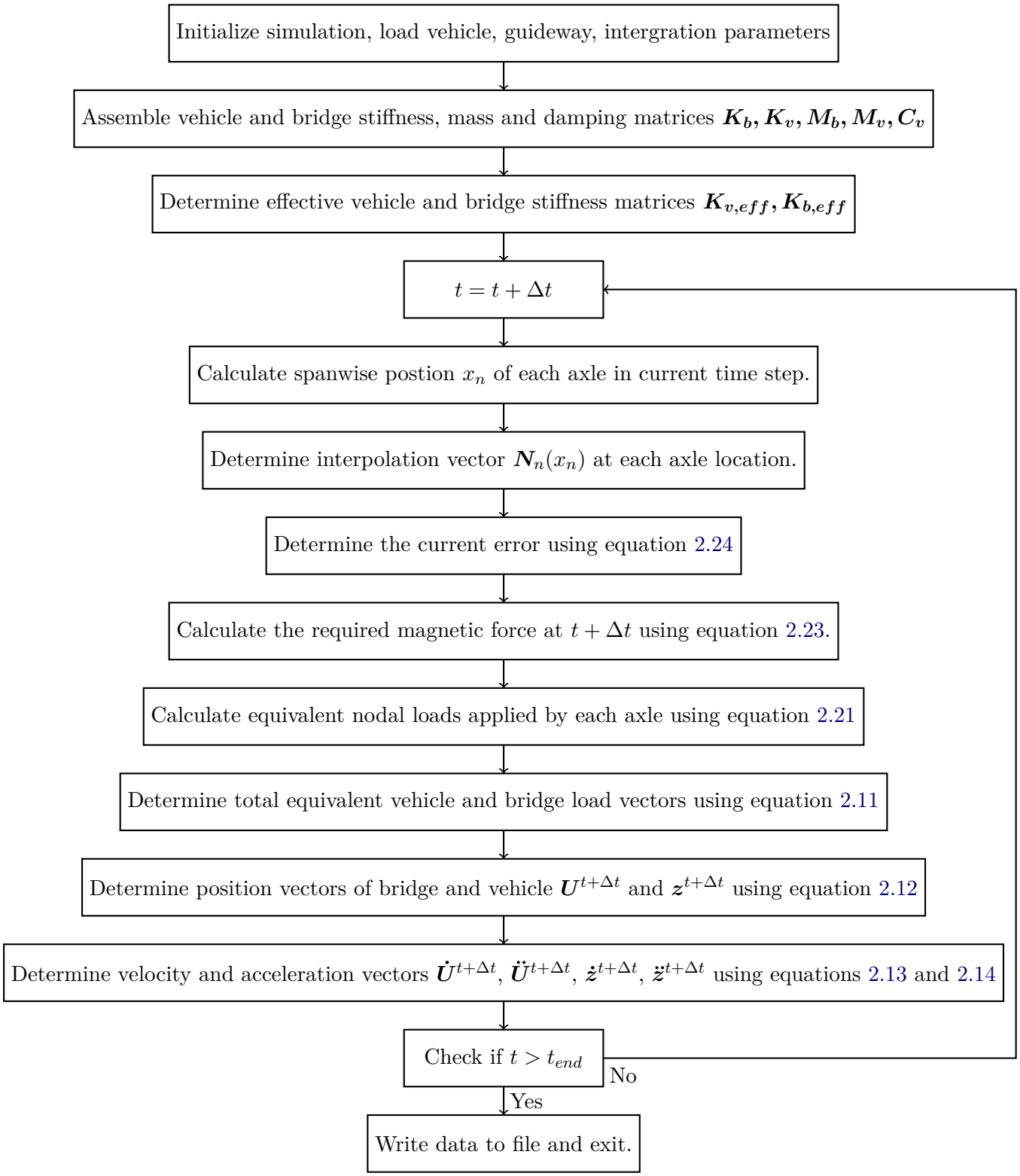

Figure 2.5: Schematic overview of solution procedure for complete model.

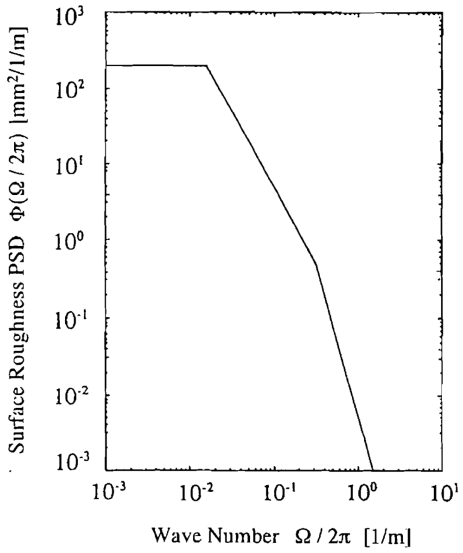

Figure 2.6: Power spectral density function of track imperfactions [31].

2.5 Guideway Imperfections

Several models for guideway, road or rail imperfections exist. The method implemented for this study, which will be described in this section, is the method implemented by Tsunashima for studying the static and dynamic performance of a maglev vehicle [31]. Since only the vertical dynamics of the vehicle are accounted for in the present study, the coupling between the left and right tracks discussed in [31] will be omitted.

As a starting point, the power spectral density (PSD) function $\Phi(\frac{\Omega}{2\pi})$ shown in figure 2.6 is assumed to be the PSD function of the track irregularities. Then the surface irregularity as function of the distance along the track x is given by equation 2.25, where N is the number of frequencies into which the frequency range is divided. $\frac{\Omega_k}{2\pi}$ is given by equation 2.26 in which $\frac{\Omega}{2\pi\,min}$ and $\frac{\Omega}{2\pi\,max}$ are the bounds of the frequency range used to generate the profile. The scaling factors a_k and b_k are random numbers from a Gaussian distribution with a zero mean and a variance σ_k given by equation 2.27. The generated imperfection profile is shown in figure 2.7, and the profile over a single span is shown in figure 2.8. The profile generated shows deviations of up to around $4.5mm$.

$$\delta_{irr}(x) = \sum_{k=1}^{N} (a_k \sin \Omega_k x + b_k \sin \Omega_k x) \tag{2.25}$$

$$\frac{\Omega_k}{2\pi} = \frac{\Omega}{2\pi\,min} + \left(k - \frac{1}{2}\right)\left(\frac{\frac{\Omega}{2\pi\,max} - \frac{\Omega}{2\pi\,min}}{N}\right) \tag{2.26}$$

$$\sigma_k = \Phi(\frac{\Omega_k}{2\pi})\left(\frac{\frac{\Omega}{2\pi\,max} - \frac{\Omega}{2\pi\,min}}{N}\right) \tag{2.27}$$

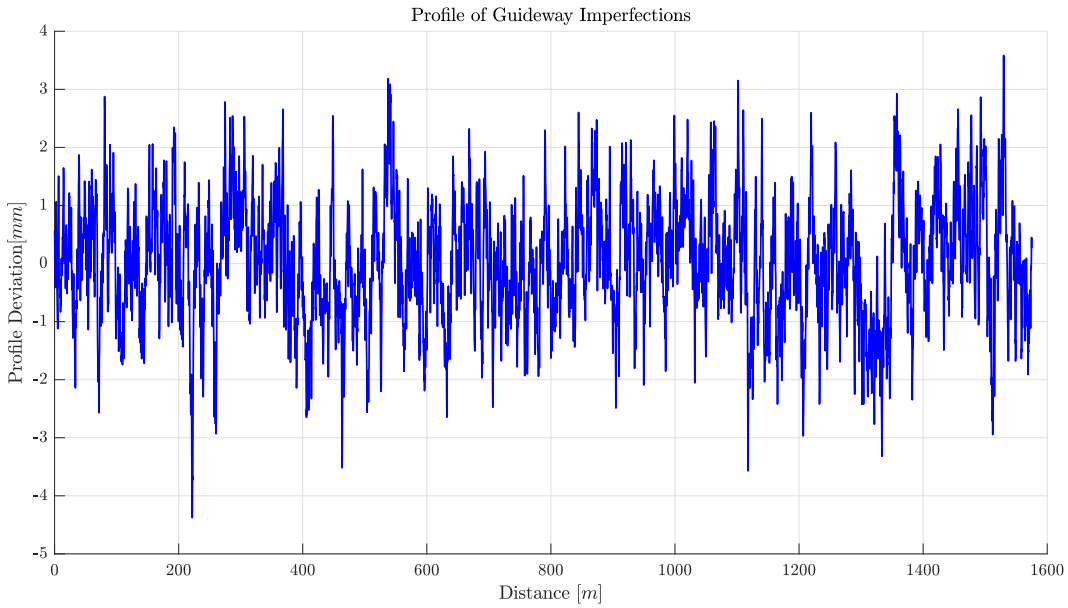

Figure 2.7: Imperfection profile generated using $N = 199901$, $\frac{\Omega}{2\pi}_{min} = 0.001$ and $\frac{\Omega}{2\pi}_{max} = 2$

Figure 2.8: Close up across a single span of imperfection profile shown in figure 2.7.

To account for the surface roughness, equation 2.24 is modified to account for the irregularity by adding the irregularity at the location of n-th axle at time t to the equation, as shown in equation 2.28. To save on computational time, the profile is pre-generated at intervals of $0.1m$, and is linearly interpolated between the discrete pre-generated points.

$$e_n^t = \boldsymbol{N}_n^T(x_n)\boldsymbol{u}_{br,n} - z_n^t + \delta_{irr}(x_n^t) \tag{2.28}$$

2.6 Parameter Estimates

To perform a reasonably efficient study of all the various influences on the dynamic behaviour of the hyperloop, a rough estimate of the expected value of the various parameters is required. This section will establish the base line hyperloop pod and track based on simple estimations of the various parameters, either from simplified physical models or using estimates generated internally by Hardt. Based on these baseline values the ranges of interest for the study will then be determined.

2.6.1 Vehicle Parameters

Looking at the model described in section 2.2, several parameters must be determined to model the pod:

- Pod mass
- Magnet mass
- Pod Inertia
- Suspension stiffness
- Suspension damping rate
- Pod dimensions
- Number of magnets

The mass of the pod has been estimated by Hardt as a function of the number of passengers, accounting for the structural mass of the pod, the passengers and their luggage, and the various systems operating within the hyperloop. This estimate also produces a vehicle estimate for the baseline, since the majority of the vehicle's length will be devoted to the seating of passengers. For a baseline pod carrying 80 passengers, this method estimates the vehicle mass as $21000kg$ with a vehicle length of $20m$ [32].

The electromagnets to be used are expected to have a lift to weight ratio of $\frac{L}{W} = 10$ **??**. Combining this with the mass estimate of $21000kg$ leads to a pod weight of $18900kg$ and a total magnet weight of $2100kg$. It is assumed for the baseline vehicle that the magnets will be spread along the length of the vehicle to better distribute the loads acting on the tube. An initial assumption is that there will be a magnet for every meter of tube length, leading to twenty $105kg$ bogies distributed evenly along the length of the vehicle.

The pod inertia is derived from the pod inertia and other vehicle parameters provided by Ren in his study on the dynamics of the Transrapid maglev train [15]. The inertia of the transrapid carriage is given as $I = 1.75 \cdot 10^6 kgm^2$ for a $24m$ long vehicle with a mass of $29200kg$. Inertia scales linearly with mass, and quadratically with distance. Using that knowledge, the inertia of the Transrapid vehicle can be scaled to find a rough estimate of the inertia of a hyperloop pod with a mass of $21000kg$ and $20m$ of length. This leads to an inertia of roughly $1 \cdot 10^6 kgm^2$.

The suspension stiffness of a vehicle may be characterized by the ride frequency of the suspension. This frequency is the fundamental frequency of the vehicle in the heave (i.e. vertical) direction. For passenger cars and trains, this frequency is generally around $1Hz$. Assuming that the actively controlled bogies provide a fairly rigid platform for the secondary suspension, the heave motion of the pod under static conditions can be simplified as a single sprung

Property	Baseline value
Pod mass	18900 kg
Magnet mass	2100 kg
Pod Inertia	$1 \cdot 10^6 kgm^{-2}$
Suspension stiffness	$7.5 \cdot 10^5$ N m^{-1}
Suspension damping coefficient	$2.4 \cdot 10^5$ kg s^{-1}
Pod length	20 m
Number of magnets	20

Table 2.2: Baseline vehicle properties

mass. The fundamental frequency of such as system is given by equation 2.29 [33]. For a fundamental frequency of $1Hz$ and a vehicle mass of $18900kg$ this leads to a spring stiffness (k) of approximately $7.5 \cdot 10^5$ N m^{-1}.

$$f_n = \frac{1}{2\pi}\sqrt{\frac{k}{m}} \tag{2.29}$$

The damping coefficient of the baseline vehicle is assumed to be the critical damping coefficient of the heave motion for the baseline vehicle. Again assuming the suspension to act as a simple mass-spring-damper system in heave, the critical damping coefficient is given by equation 2.30 [33]. For the given mass and spring stiffness, the damping coefficient is then $2.4 \cdot 10^5$ kg s^{-1}. The complete set of vehicle properties is summarized in table 2.2.

$$c_c = 2\sqrt{km} \tag{2.30}$$

2.6.2 Tube Parameters

Based on the tube model described in section 2.3, the following parameters of the tube must be determined:

- Section stiffness
- Material density
- Cross sectional area
- Poisson ratio
- Span length

The current design of the hyperloop as envisioned by Hardt calls for a tube with a $4m$ diameter, made out of a tubing steel alloy conforming to the ISO 3183:2012 norm for pressure vessels. Using the material properties of this steel, the minimal thickness of the tube under the nominal pressure conditions in the tube is found to be approximately 20mm [32]. Using this thickness the second moment of area can be determined as $0.5m^4$. The cross sectional area is $0.5m^2$. The remainder of the material properties are summarized in table 2.3. The expected span length, based on the infrastructure proposed in the white paper of Elon Musk, is around 35m [2].

Property	Baseline value
E	$210GPa$
I	$0.5m^4$
Span length	$35m$
ρ	$7800kgm^{-3}$
A	$0.5m^2$

Table 2.3: Baseline tube properties

Gain	value
K_p	$1.59 \cdot 10^8$
K_i	$1.73 \cdot 10^{10}$
K_d	$9.70 \cdot 10^5$

Table 2.4: Baseline vehicle controller gains

2.6.3 Controller Gains

The controller gains were chosen using the Ziegler-Nichols method of control tuning [34], where the integral and derivative gains K_i and K_d are chosen based on the value of proportional gain K_p for which the system is marginally stable (i.e. further increases in K_p will lead to an unstable system) when K_i and K_d are zero. This value of K_p was determined manually. After setting the gains to the values determined using the Ziegler-Nichols method, the controller was manually tuned to reduce the settling time of the system after a step input. This lead to a system with a lot of overshoot but a very short settling time, which leads to a system that rapidly adapts to disturbances. The gains used in this study are summarized in table 2.4. These are the gains for a single axle vehicle. Since the controller is a linear system, the gains for a multi axle vehicle are simply the gains in table 2.4 divided by the number of axles. The displacement response of a single bogie to a step input is shown in figure 2.9.

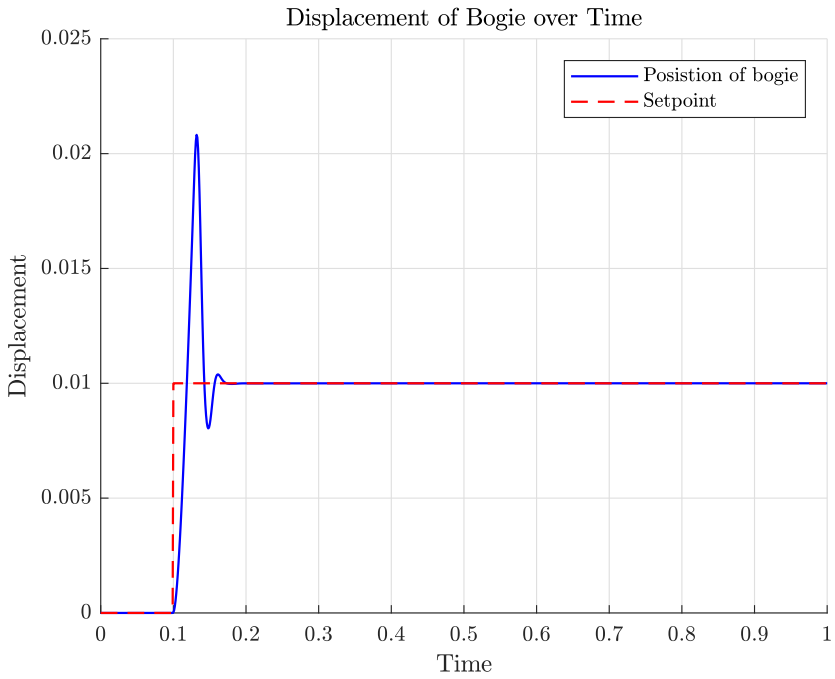

Figure 2.9: Step response of baseline vehicle bogie using baseline controller gains.

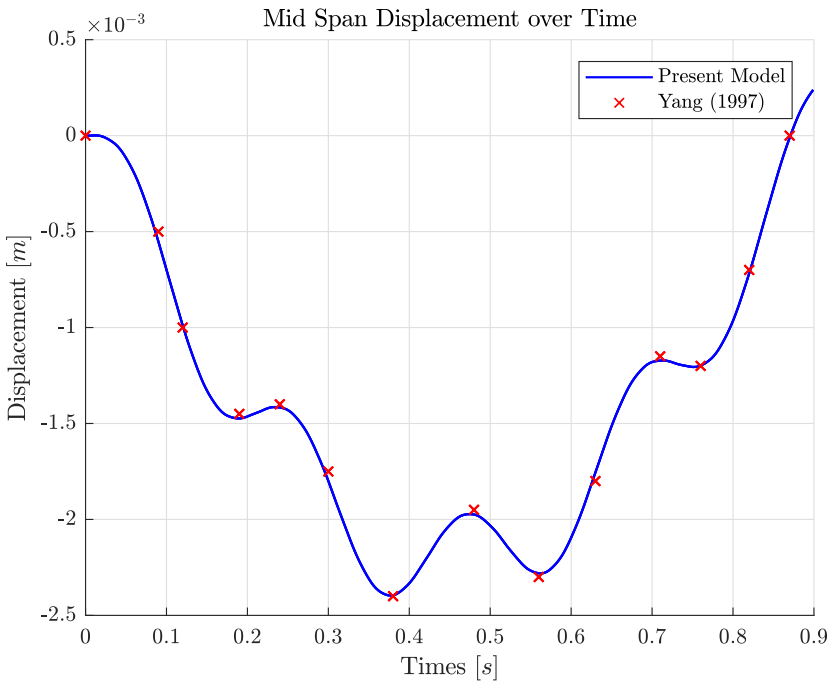

Figure 2.10: Comparison of mid span displacement over time for present guideway model and the model created by Yang for the case presented by Yang [1]

2.7 Model Verification

To verify the the accuracy of the model, it is important to recognize that the model effectively consists of three parts: The guideway, the vehicle and the PID-controller linking the vehicle to the guideway. If the guideway model can correctly determine the dynamic response of the guideway to a moving (series of) forces, the vehicle model can correctly predict the motion of the vehicle based on a set of input forces acting on the bogies and the PID controller can correctly set $\boldsymbol{F}_{t+\Delta t}$ to control the distance between the bogies and the guideway, the system as a whole will function correctly. The accuracy of the three components of the simulation can therefore be established independently, and only the correct interaction between the different components needs to be verified using the complete model.

2.7.1 Guideway Model

The guideway model consists of a finite element representation of the tube, which is loaded by a moving force or series of forces. The guideway model is employed to calculate the dynamic response of the case presented by Yang [1]. The results generated by the present model as well as the data generated by Yang are shown in figure 2.10. The generated results and the data presented by Yang are in good agreement.

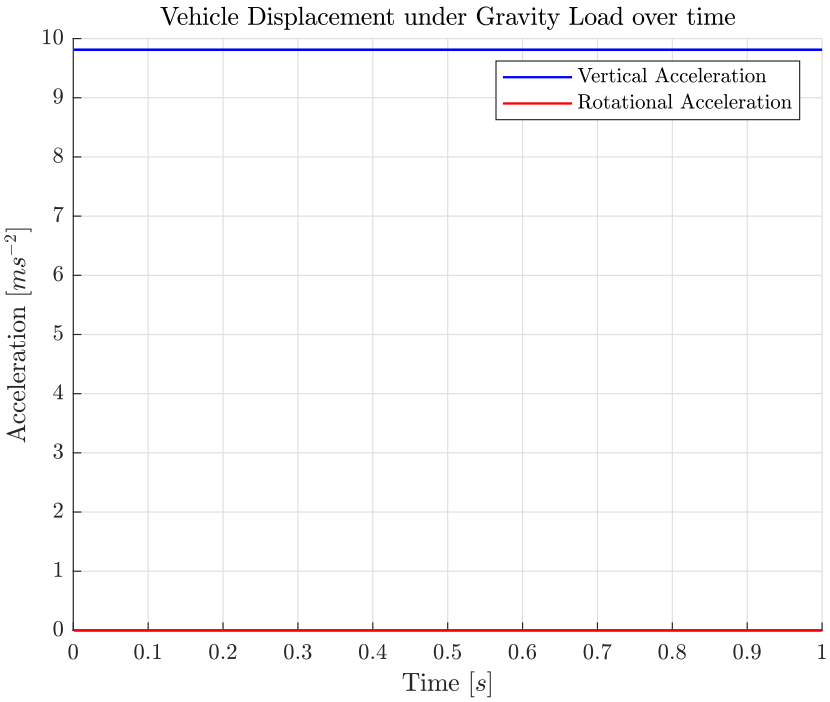

Figure 2.11: Vehicle verification results, acceleration of vehicle under pure gravity load.

2.7.2 Vehicle Model

To verify the accuracy of the vehicle model, a $1m$ long two axle vehicle with 1kg mass for the bogies and body, $1kgm^{-2}$ body inertia, and a $1Nm^{-1}$ spring stiffness is simulated. Several cases are simulated to verify the correct behaviour of the vehicle model: A free fall of the vehicle under only the load of gravity, the free vibration of the body with the bogies held in place, the free vibration of the bogies with the body held in place, an upwards motion as a result of a load double the gravity load applied to the bogies and a simulation of the rotational vibration of the body with the bogies held in place. The results of these simulations are shown in figures 2.11-2.15

From these figures, it follows that the vehicle model behaves as expected. From figure 2.11 it is clear that under pure gravitational load the model correctly integrates the acceleration of the vehicle to $9.81ms^{-2}$, and that there is no rotation in the vehicle body. Figure 2.12 shows the free vibration of the vehicle body, which using equation 2.29 should have a frequency of $0.225Hz$ and therefore a period of $4.44s$. This matches exactly with the simulated oscillation. Similarly, equation 2.29 predicts a frequency of 0.159Hz and a period of 6.28s for the free vibration of the bogie, which again matches the vibration simulated using the vehicle model shown in figure 2.13.

2.7.3 PID Controller

The correct operation of the PID controller is verified by controlling the position of a unit mass using the force control method outlined in section 2.4, in the presence of various disturbing

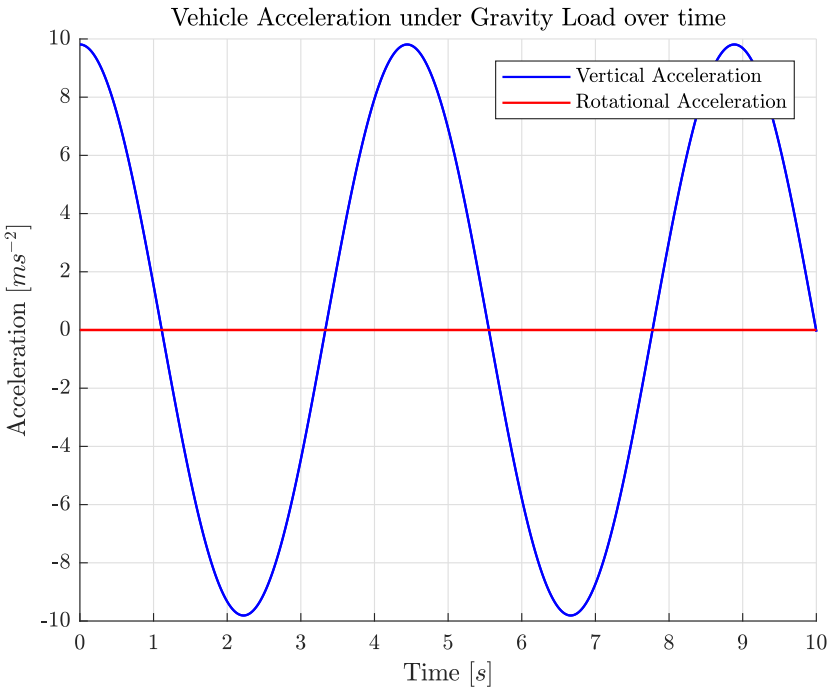

Figure 2.12: Vehicle verification results, free vibration of vehicle body from zero initial condition.

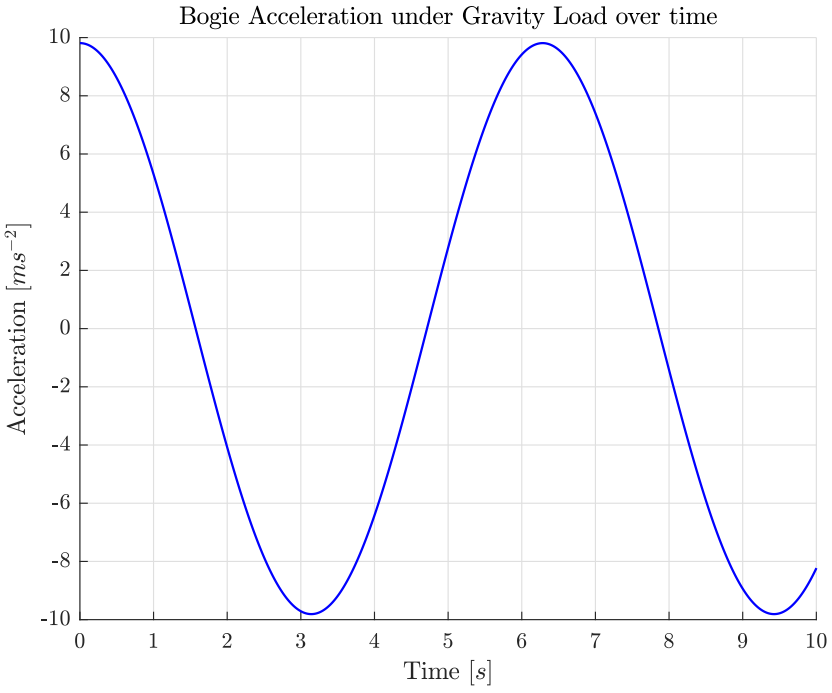

Figure 2.13: Vehicle verification results, free vibration of vehicle bogie from zero initial condition.

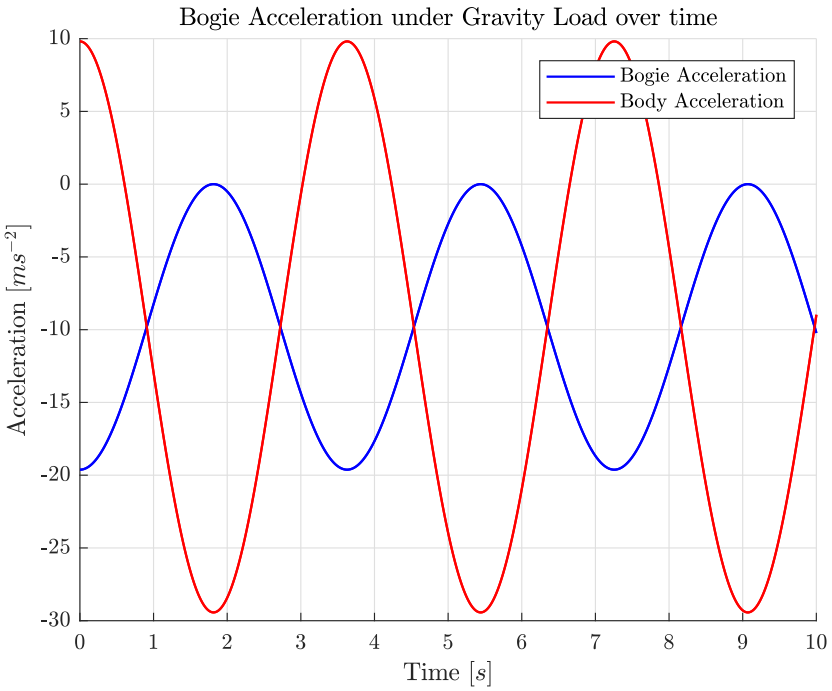

Figure 2.14: Vehicle verification results, vibration of vehicle body and bogie under combination of gravity load acting on complete vehicle and double the total vehicle weight acting on the bogies only opposing the gravity load.

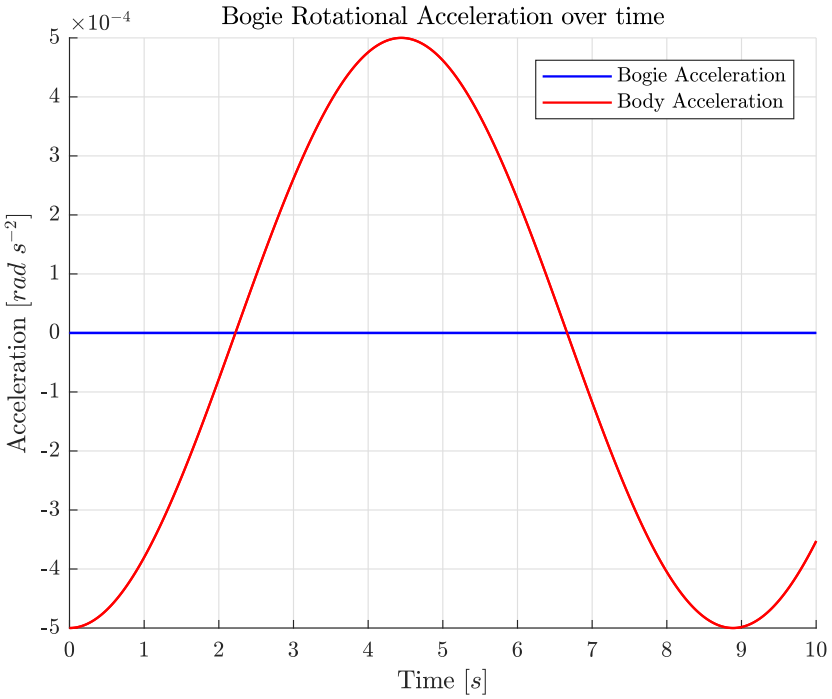

Figure 2.15: Rotational vibration of vehicle body after release from $0.001\ rad$ initial angle.

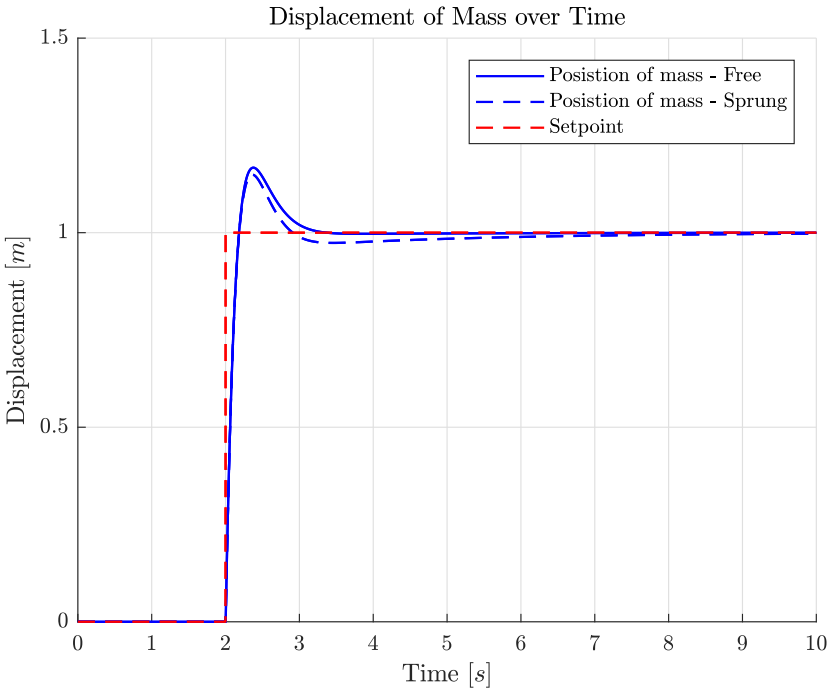

Figure 2.16: Step response of mass under force based PID-control for both a free mass and a sprung mass.

forces and set-point irregularities. Figure 2.16 shows the response of both a mass and a mass-spring system to a step input in its set-point. The controller is shown to be functional and controls the position of the mass to its new set-point using a force input. Figure 2.17 shows the response of the spring-mass system to a sinusoidal input in set-point, with a gravitational load applied, and both with and without a disturbing force of $F_d = F_g \sin(3t)$ to simulate an oscillating vehicle. Without the disturbance force, the set-point is followed exactly, while the disturbance force leads to a small oscillation around the set-point. The controller outlined in section 2.4 is therefore proven to be a functional PID-controller which will output the force required for both the vehicle model and the guideway model.

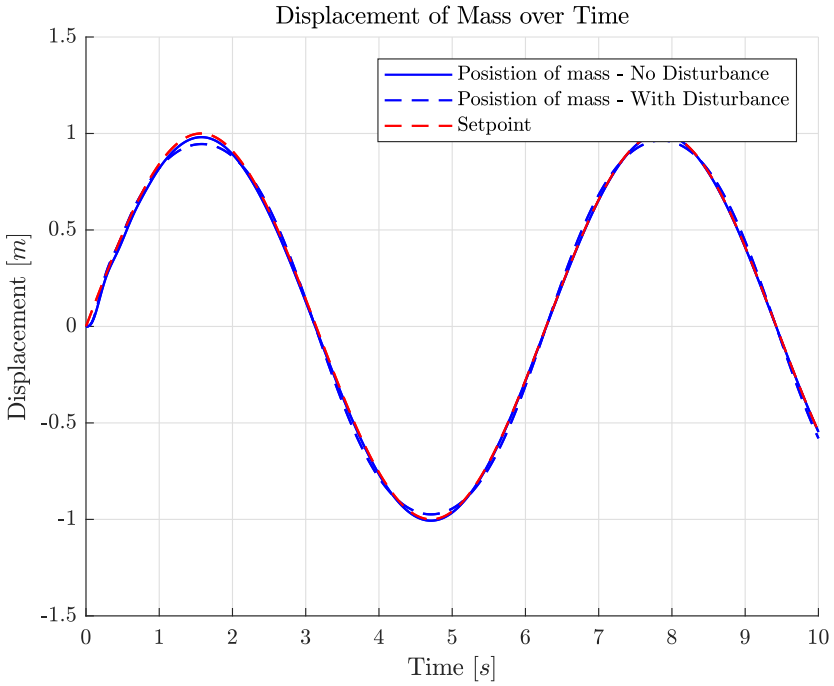

Figure 2.17: Response of sprung mass under gravitational loading to force based PID-control with sinusoidal set-point variation, with and without harmonic disturbing force.

Chapter 3

Results

The results of the dynamic simulations of the reference vehicle will be laid out in this chapter. The dynamic response of the baseline vehicle will be shown, and the effect of varying the baseline design will be investigated. All simulations have been carried out with the baseline vehicle and tube except for the specific parameters varied in each of the subsections in this chapter. All simulations were carried out with an integration time step of $\Delta t = 1ms$.

The baseline vehicle with the parameters determined in chapter 2 has been simulated to run over a continuous stretch of forty five spans of the baseline tube. Some results of this simulation are shown in figures 3.1 - 3.6. For these figures one can see that it takes some time for the vehicle to settle into a steady state motion after entering the simulated tube. After around one second of running, the vehicle bogies and body are moving in a steady heave motion. The pitch oscillation takes somewhat longer to settle as evidenced by figure 3.4. At the end of the domain, another small peak can be observed in all results.

Looking at the accelerations of the body and the bogies, the main component of the vibrations has a period of $0.117s$. This is equal to the time it takes to cross the $35m$ span when travelling at $300ms^{-1}$. The bogies also show the presence of a higher frequency component in the vehicle response, while the secondary suspension damps this higher frequency out of the movement of the vehicle body.

The deflection of the tenth span crossed by the vehicle over time, shown in figure 3.3, has a maximum that is 1.52 times the maximum deflection of the tenth span under the static vehicle load.

The magnetic forces required to keep the bogies at their requested setpoint are shown in figure 3.5. The magnet force fluctuates around the weight carried by each magnet by roughly 2.5%. This force variation is sufficient to keep the steady state air gap variations very low, at around $30\mu m$ as can be observed in figure 3.6. It is important to note here that the magnetic force variations occur with the crossing frequency of the vehicle, and that it can reasonably be expected for the magnetic systems of the pod to keep up with these fluctuations.

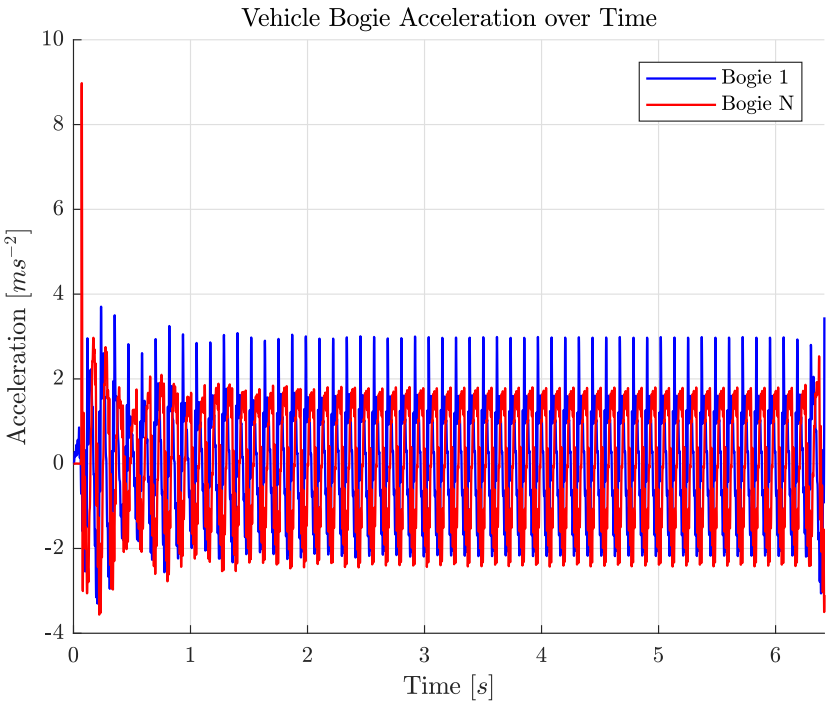

Figure 3.1: Baseline vehicle front and rear bogie acceleration over time.

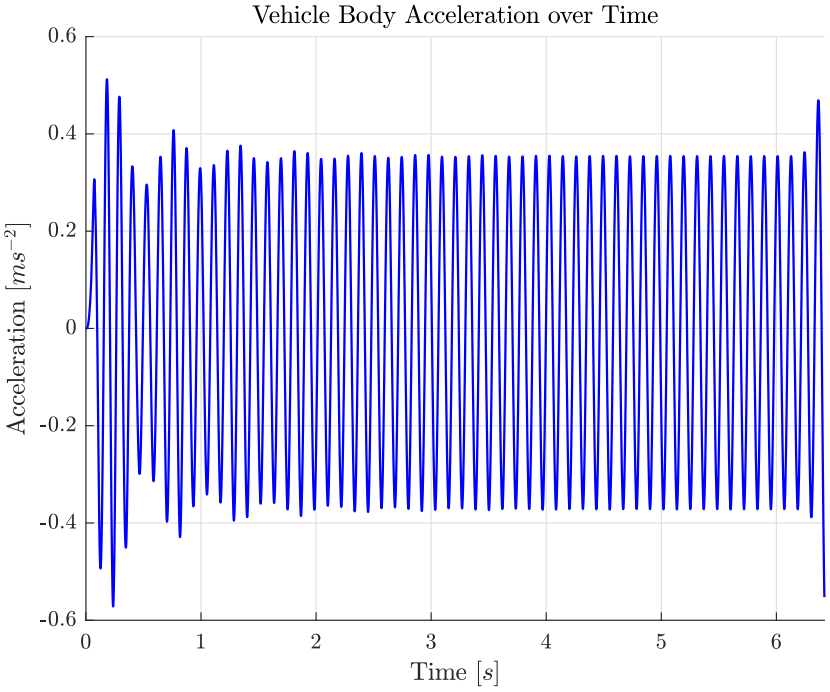

Figure 3.2: Baseline vehicle body acceleration over time.

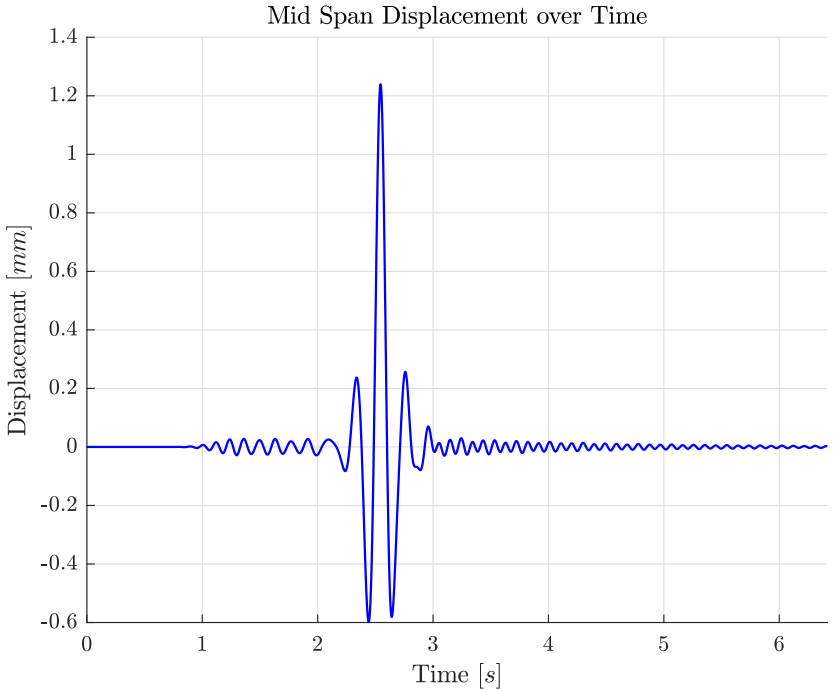

Figure 3.3: Baseline vehicle midspan displacement of tube over time.

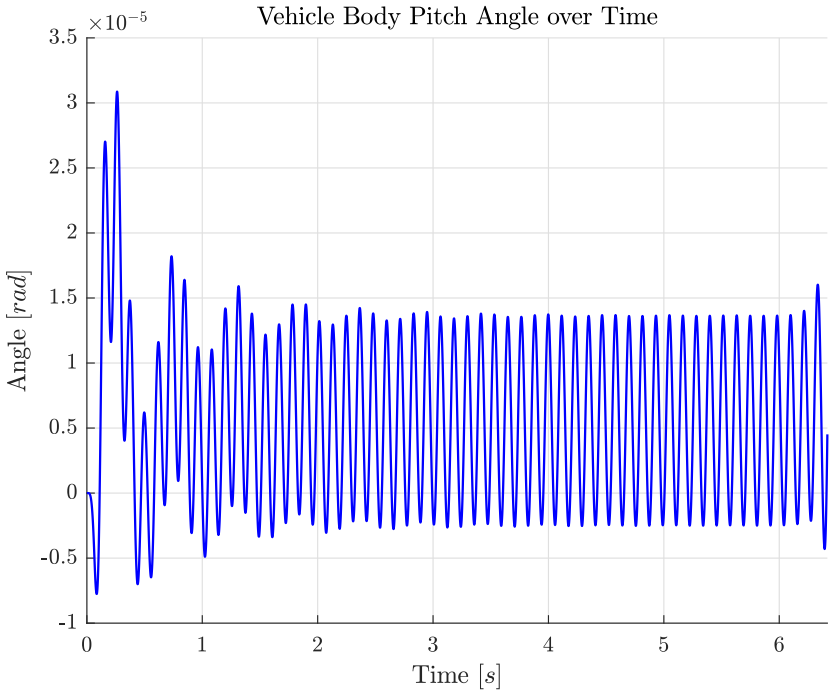

Figure 3.4: Baseline vehicle body pitch angle over time.

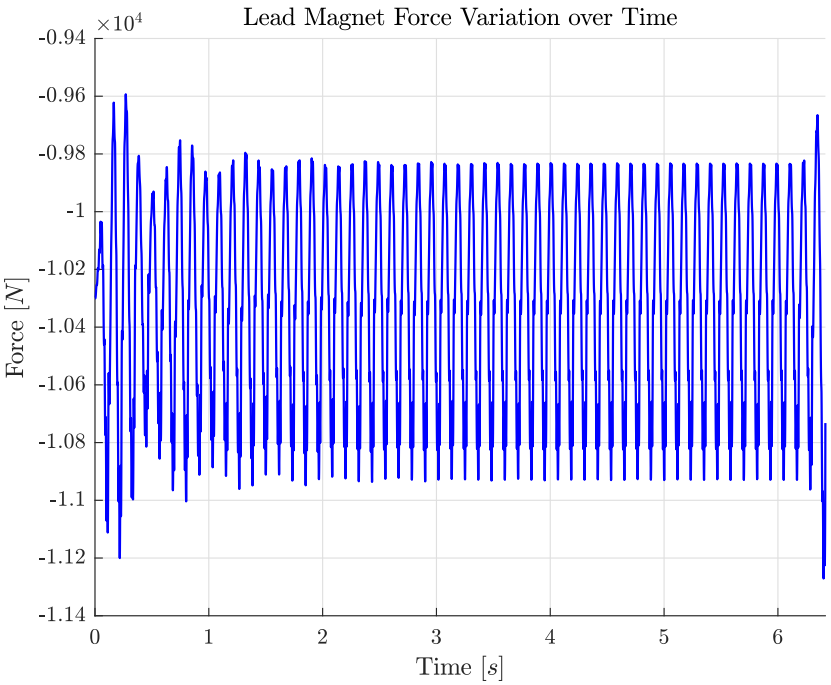

Figure 3.5: Lead magnet force variation over time for baseline vehicle.

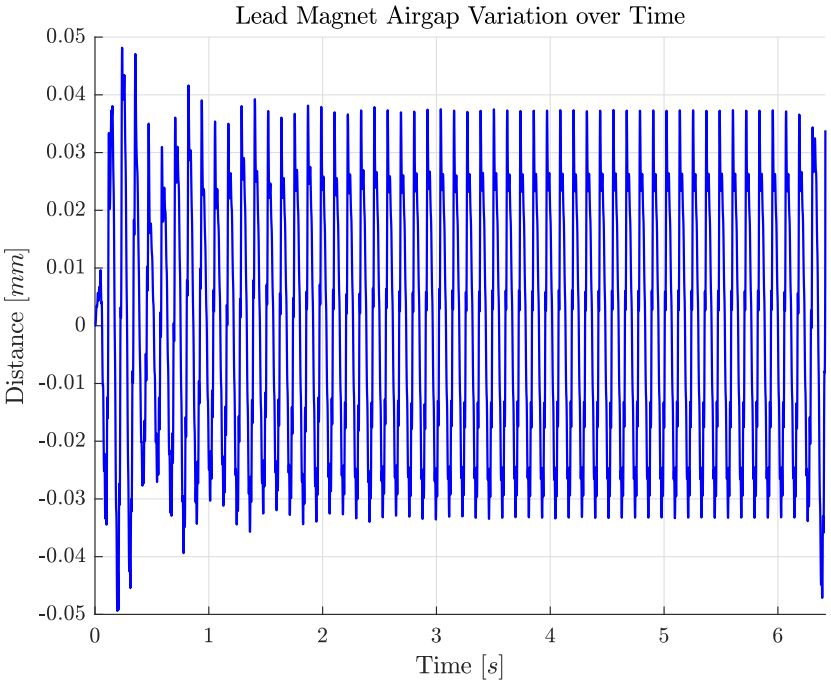

Figure 3.6: Baseline vehicle air gap variation of lead magnet.

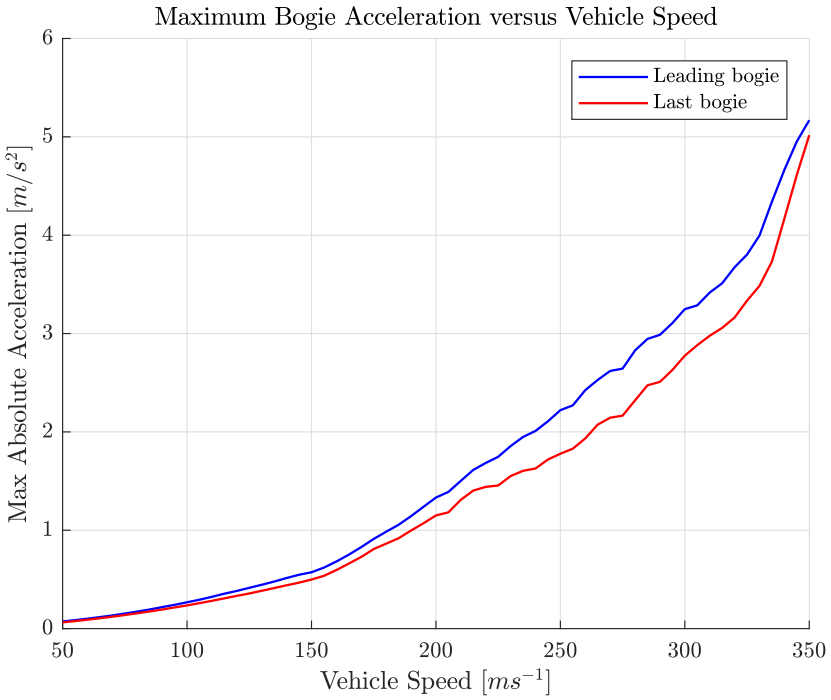

Figure 3.7: Maximum acceleration of first and last bogie at various vehicle velocities.

3.1 Effect of Varying Vehicle Parameters

3.1.1 Vehicle Speed

The maximum cruising speed of the vehicle is expected to be around $300ms^{-1}$. Since this speed may change due to operational demands, such as sections of track where small radius corners are required, the dynamic behaviour over a range of speeds will be investigated. The maximum acceleration of the bogies, the maximum body acceleration and the maximum mid span deflection are plotted over a range of velocities from $50ms^{-1}$ to $350ms^{-1}$ in figures 3.7-3.9.

As the vehicle speed is increased, the accelerations of the bogies rise dramatically, increasing by nearly two orders of magnitude at high velocities compared to the low speed cases. Due to the presence of a secondary suspension, the increase in acceleration isn't nearly as dramatic for the vehicle body. Despite this, the highest velocity still leads to an absolute maximum acceleration increase of an order of magnitude compared to the slowest case looked at.

The mid span deflection increases with speed. The increase is less dramatic than the increase in accelerations on the vehicle, although still very significant. Increasing the velocity of the vehicle from $50ms^{-1}$ to $350ms^{-1}$ leads to an increase of 102% in maximum deflection.

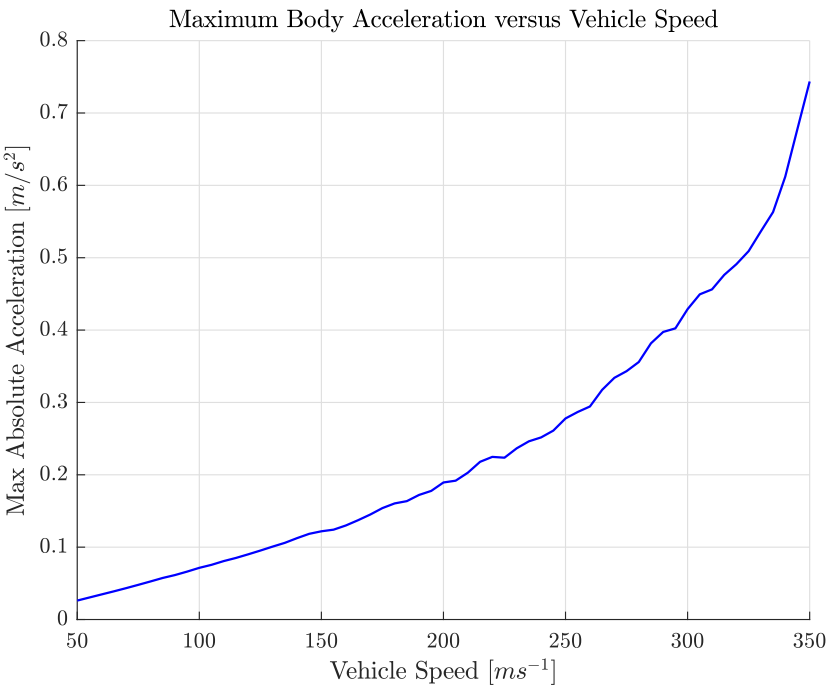

Figure 3.8: Maximum acceleration of vehicle body at various vehicle velocities.

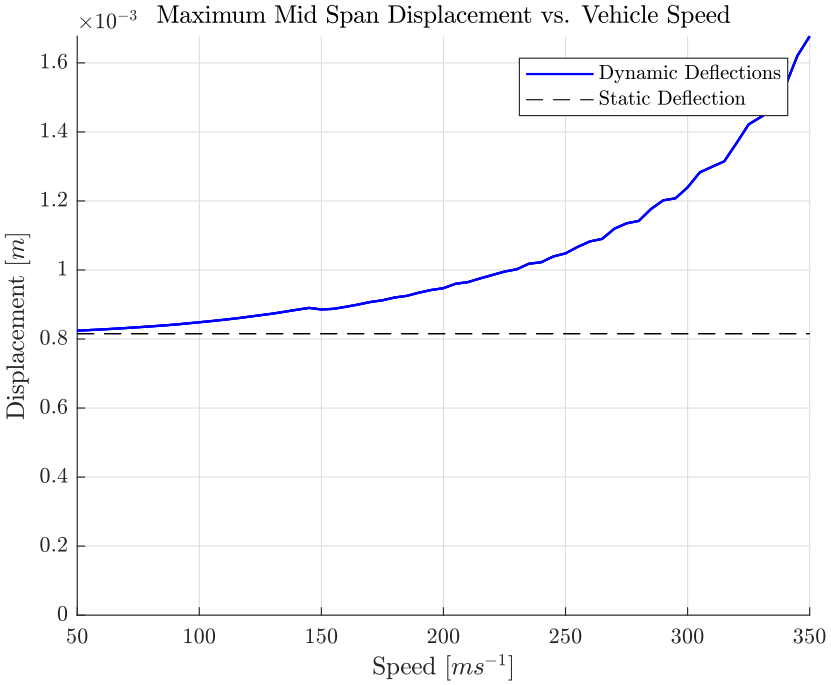

Figure 3.9: Maximum displacement of tube midspan at various vehicle velocities.

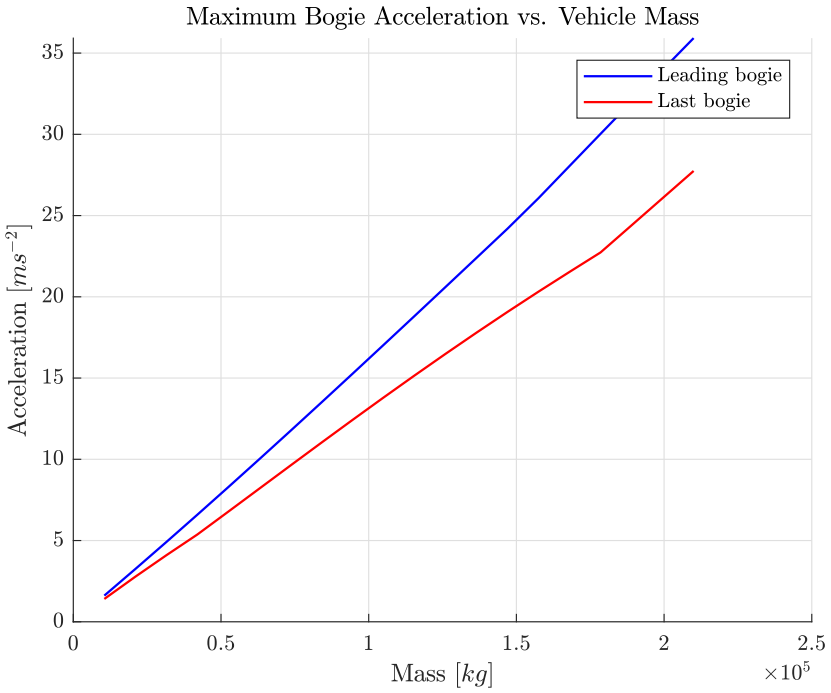

Figure 3.10: Vehicle bogie acceleration versus total vehicle mass.

3.1.2 Vehicle Mass

The vehicle may turn out lighter or heavier than the original estimates made by Hardt. The effect of changes in mass is investigated by varying the complete vehicle mass from $10500kg$ to $210000kg$, or from $0.5\times$ the baseline mass to $10\times$ the baseline mass. To ensure a one to one comparison between the various cases, the dynamic system resting on the magnets must have identical dynamic properties regardless of the mass of the vehicle. That means it must be a critically damped system with a $1Hz$ heave frequency. Looking at equations 2.29 and 2.30, this means that the vehicle spring rate and damping rate must be redetermined for each mass to ensure a one to one comparison.

The results are shown in figures 3.10 - 3.12. The accelerations of the bogies and body as well as the maximum displacement of the mid span of the tube show linear increase with increasing mass.

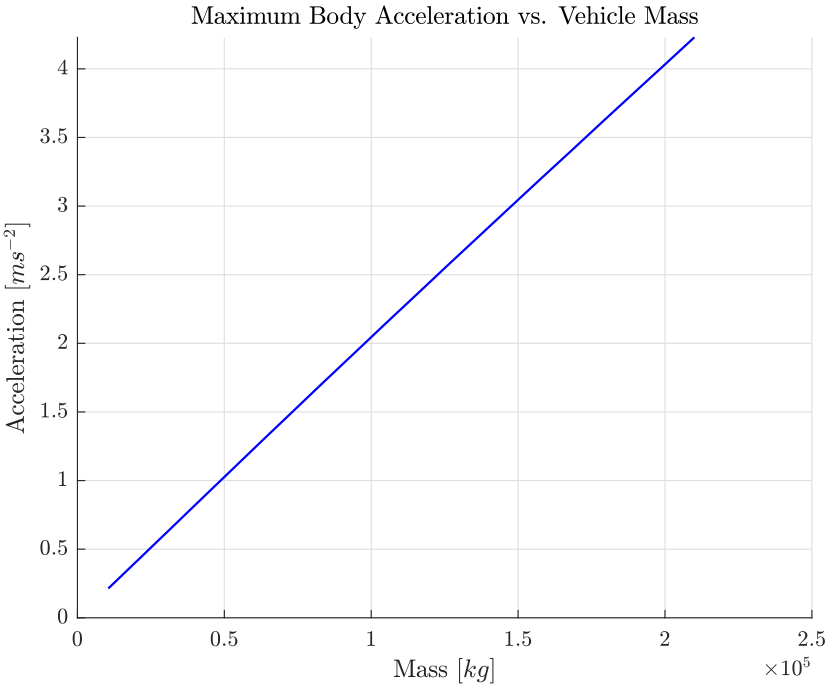

Figure 3.11: Vehicle body acceleration versus total vehicle mass.

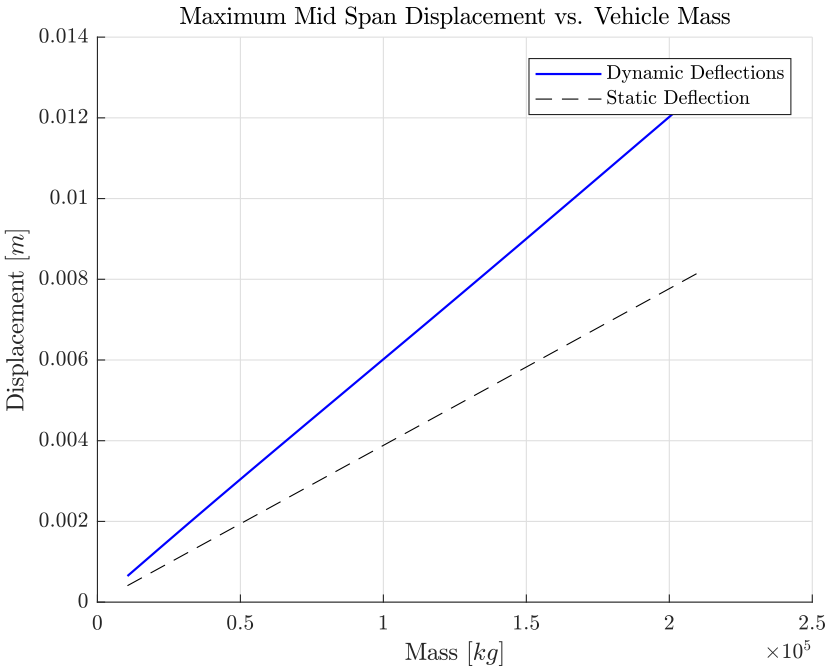

Figure 3.12: Maximum mid span displacement versus total vehicle mass.

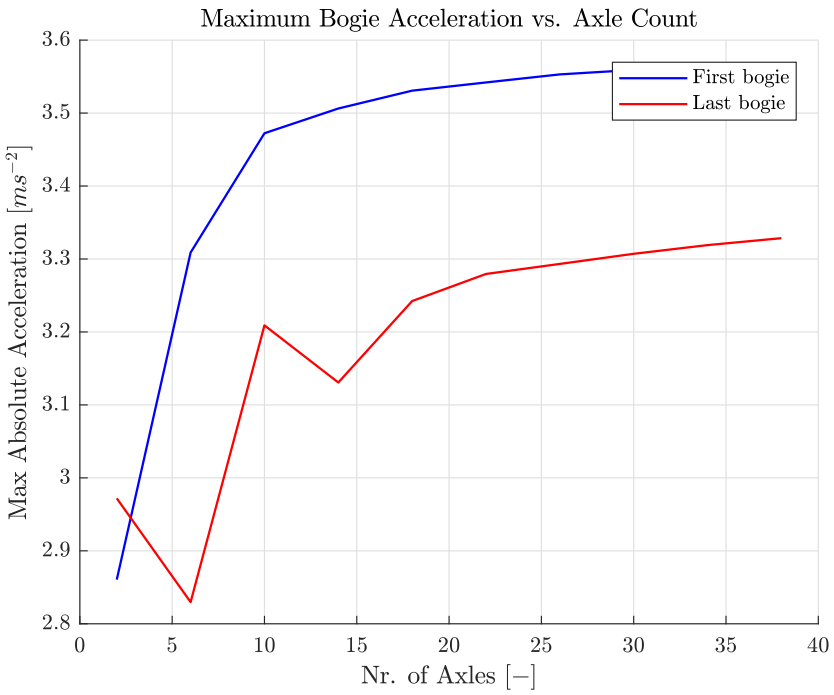

Figure 3.13: Maximum acceleration of first and last bogie for varying numbers of axles.

3.1.3 Number of Axles

The number of axles the vehicle possesses will have a direct influence on the complexity of the vehicle as a whole. A minimum of two axles is required to create a pitch stable vehicle. For this comparative analysis, a maximum of forty axles will be examined. This leads to a vehicle with a bogie every $0.5m$ and a fairly evenly distributed loading on the tube. The maximum accelerations experienced by the first and last bogie, the maximum acceleration of the body and the maximum deflection of the tube are plotted against the number of axles in figures 3.13-3.15.

The accelerations and displacement all show a steep upward trend when increasing the number of axles from a basic two axle vehicle. As the number of axles is increased and the load becomes more distributed the effect levels out.

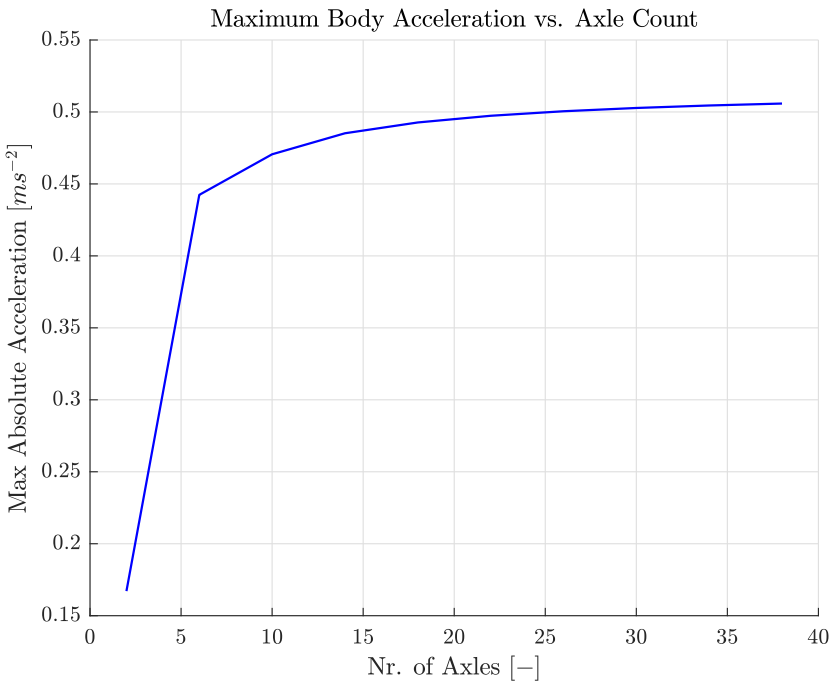

Figure 3.14: Maximum acceleration of vehicle body for varying numbers of axles.

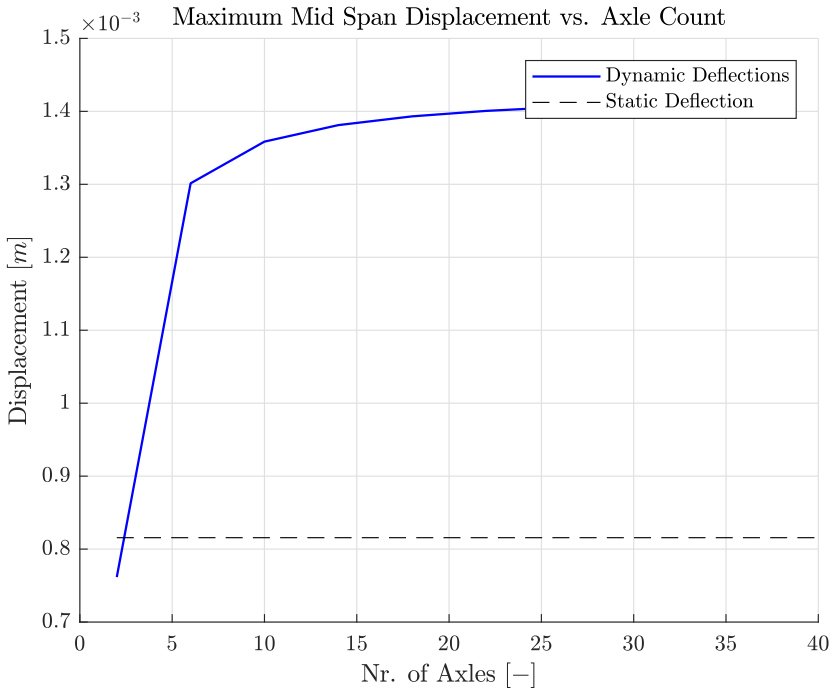

Figure 3.15: Maximum displacement of midspan for varying numbers of axles.

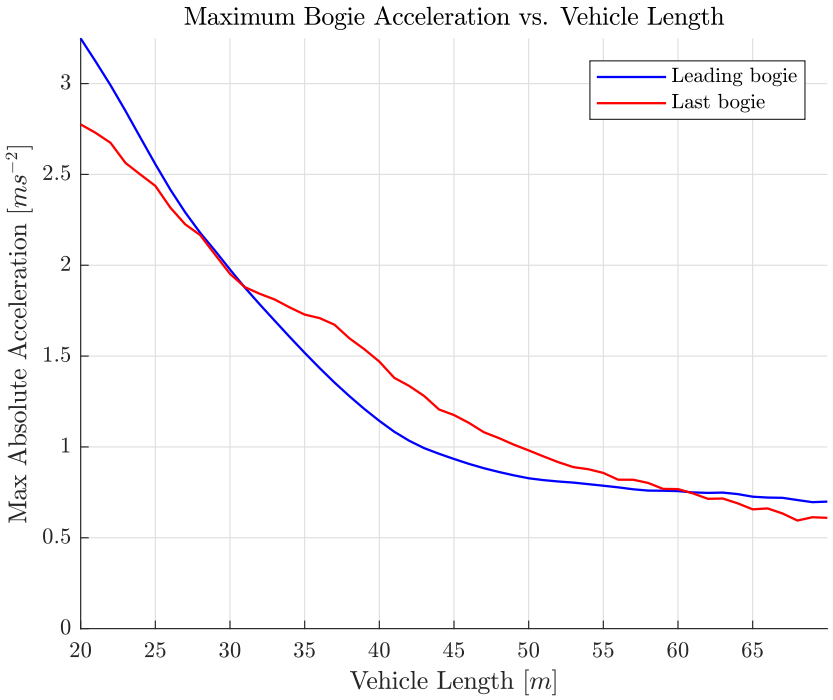

Figure 3.16: Maximum bogie acceleration of lead and last bogie for various vehicle lengths.

3.1.4 Vehicle Length

Increasing the vehicle length will change the distribution of the load exerted by the vehicle on the tube. Looking at vehicle form $20m$ to $70m$ in length, the results for bogie acceleration, body acceleration and maximum midspan displacement are given in figures 3.16-3.18. The number of axles is held constant for these simulations.

The results show a clear decrease in accelerations for the bogies and body as a results of the increase in vehicle length, as well as a decrease in mid span displacement for longer vehicles. The acceleration of the bogies declines sharply upon the initial increase in length, while the decrease is significantly slower with further increases in vehicle length when the vehicle is longer than $45m$. The body accelerations also sharply decrease for the initial increases in vehicle length, and are at a minimum for vehicles $48m$ long. After this minimum, the body accelerations increase slightly until a local maximum for $60m$ long vehicle. The mid span displacement decrease quickly but flatten out for vehicles approaching lengths of $70m$, or double the span length.

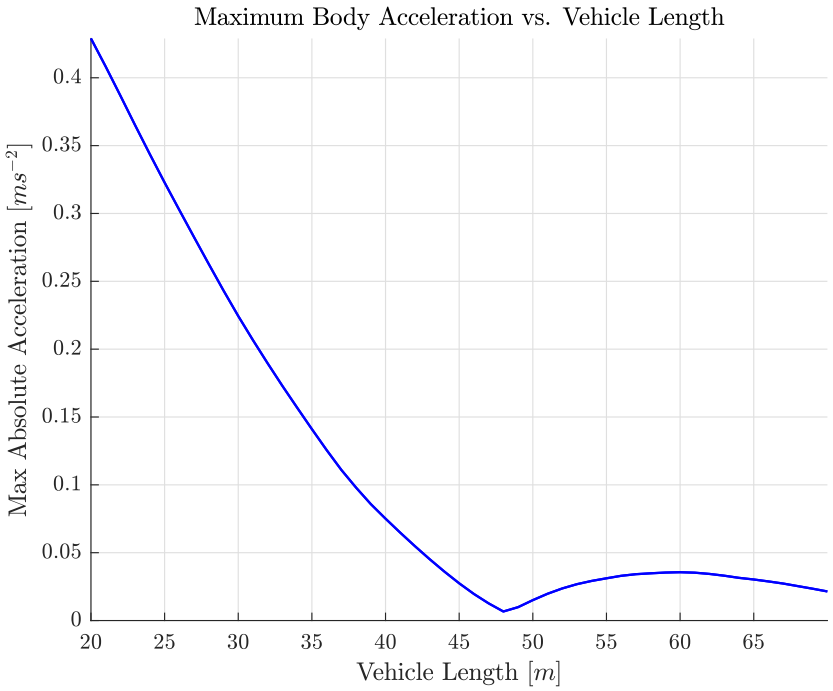

Figure 3.17: Maximum acceleration of vehicle body for various vehicle lengths.

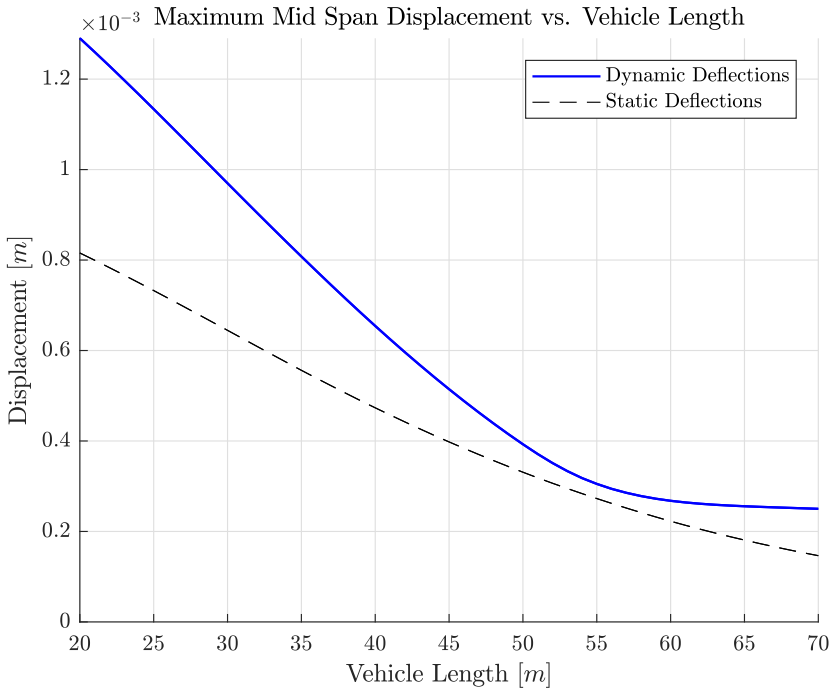

Figure 3.18: Maximum mid span deflection for various vehicle lengths.

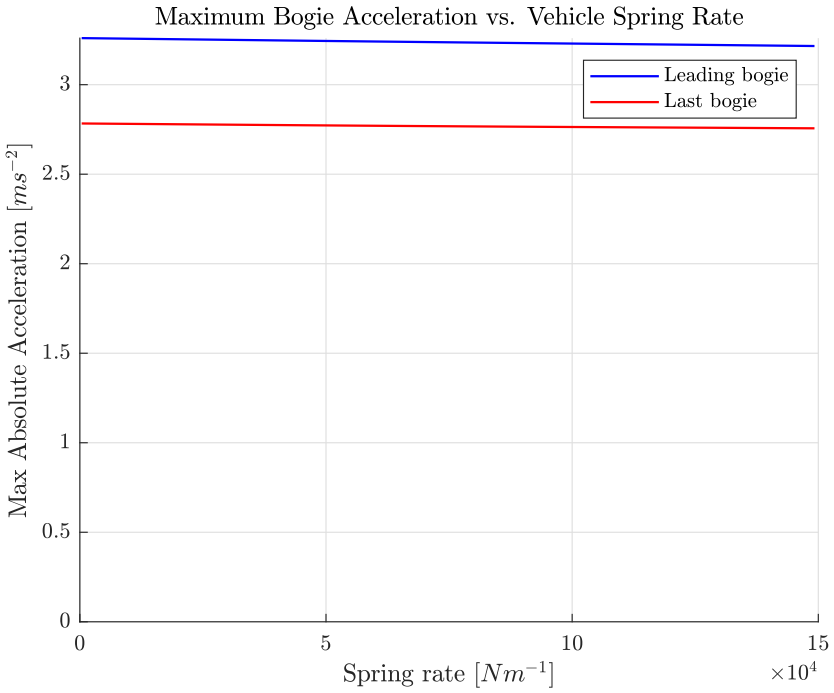

Figure 3.19: Maximum acceleration of front and rear bogies versus secondary suspension spring stiffness.

3.1.5 Spring Rate

The vehicle spring rate of the baseline vehicle is chosen in such a way that the ride frequency is $1Hz$, in line with passenger vehicles in other modes of transportation. The spring stiffness is varied from 0.1 to 4 times the baseline spring stiffness. The results are shown in figures 3.19-3.21.

The effect of varying the spring stiffness is fairly small for the bogie acceleration and the mid span displacements of the tube, with around a 1% difference in bogie acceleration at the extremes of the range and a difference in maximum displacement of around 0.5%. The effect on the maximum acceleration of the body is more significant, with around 10% difference between the highest and lowest body accelerations within the range of calculations. It should be noted that at the lower extreme of the range, the static deflection of the pod under gravity loading becomes very high (on the order of $2m$) and the viability of using such soft springs has to be questioned.

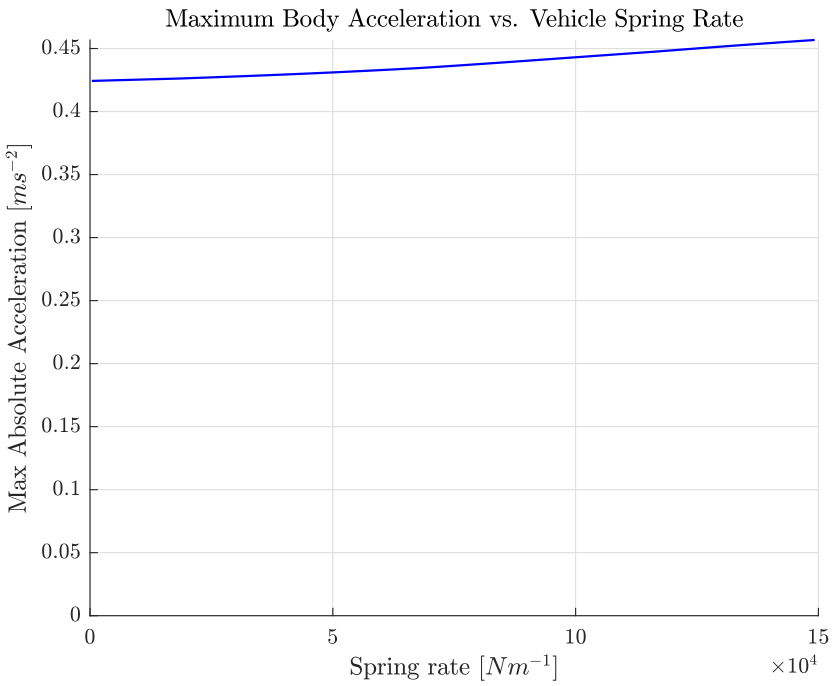

Figure 3.20: Maximum acceleration of vehicle body versus secondary suspension spring stiffness.

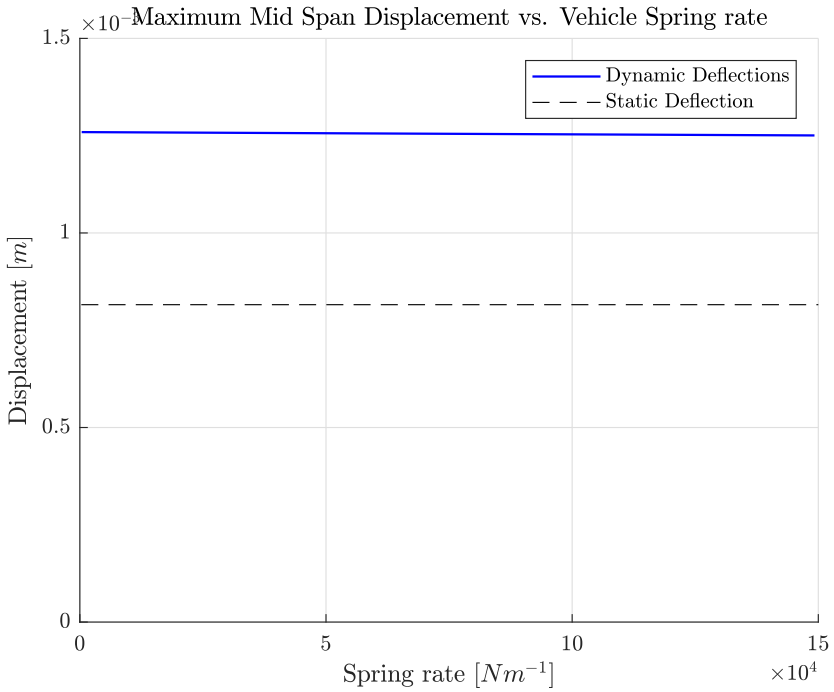

Figure 3.21: Maximum mid span displacement versus secondary suspension spring stiffness.

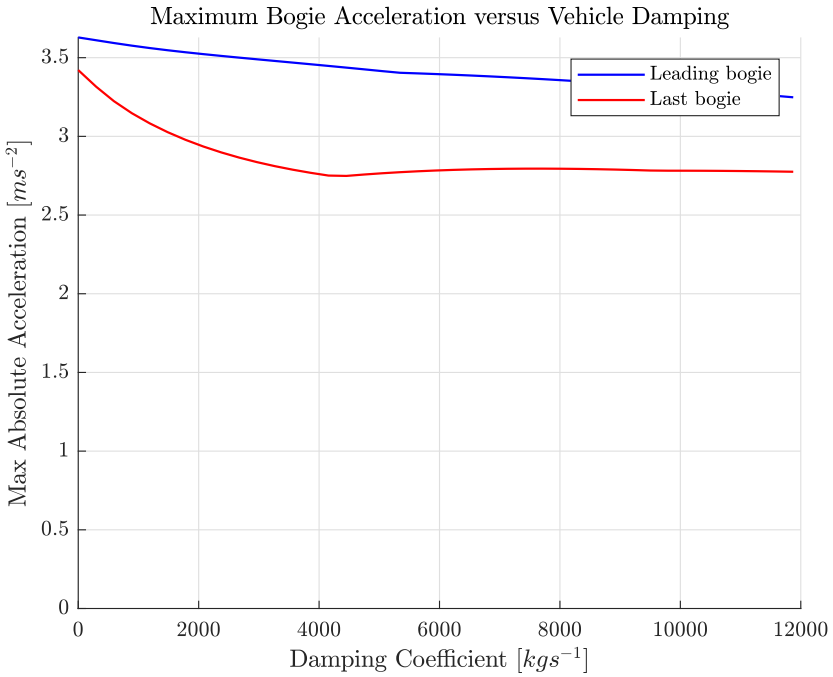

Figure 3.22: Front and rear bogie accelerations plotted against various secondary suspension damping rates.

3.1.6 Damping rate

The baseline vehicle is critically damped. The effect of damping on the dynamic performance of the vehicle will be examined by sweeping through damping coefficients. The range starts with the undamped solution, and ends with an critically damped suspension. The results are shown in figures 3.22-3.24.

The effect on the maximum deflection of the bridge is negligible, with less than 1% difference between the maximum and minimum within the examined range. The effect on the acceleration of the bogies is more pronounced, showing a fairly linear drop off in acceleration of the front bogie, with a roughly 4% decrease in acceleration when comparing the undamped case and the maximum damping case. The rear bogie shows an even steeper drop of, with around 17% lower acceleration at the end of the examined range. The acceleration of the body shows a slight drop as the damping is increased, but this trend reverses at a fairly low damping coefficient, and as the damping is increased further the acceleration of the body starts increasing linearly with the damping ratio.

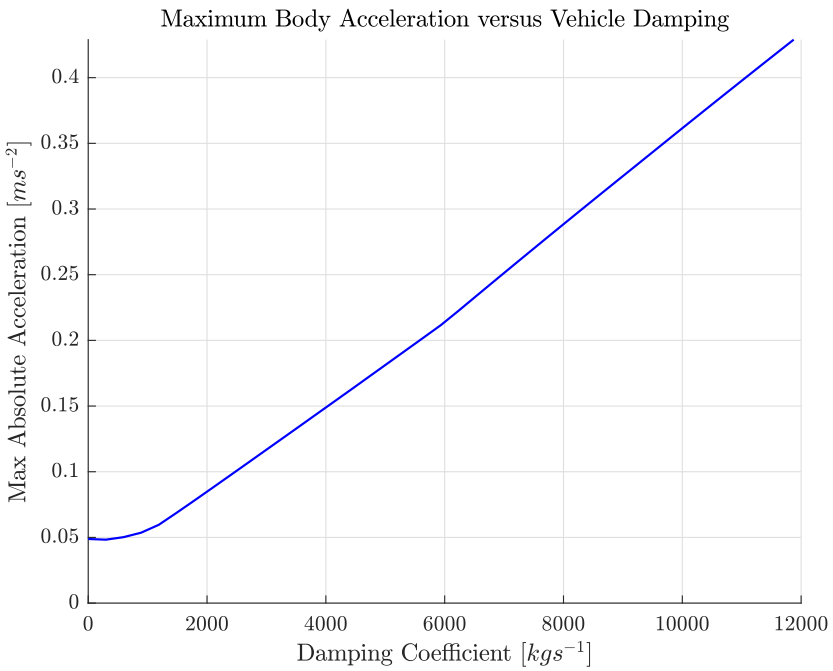

Figure 3.23: Vehicle body accelerations plotted against various secondary suspension damping rates.

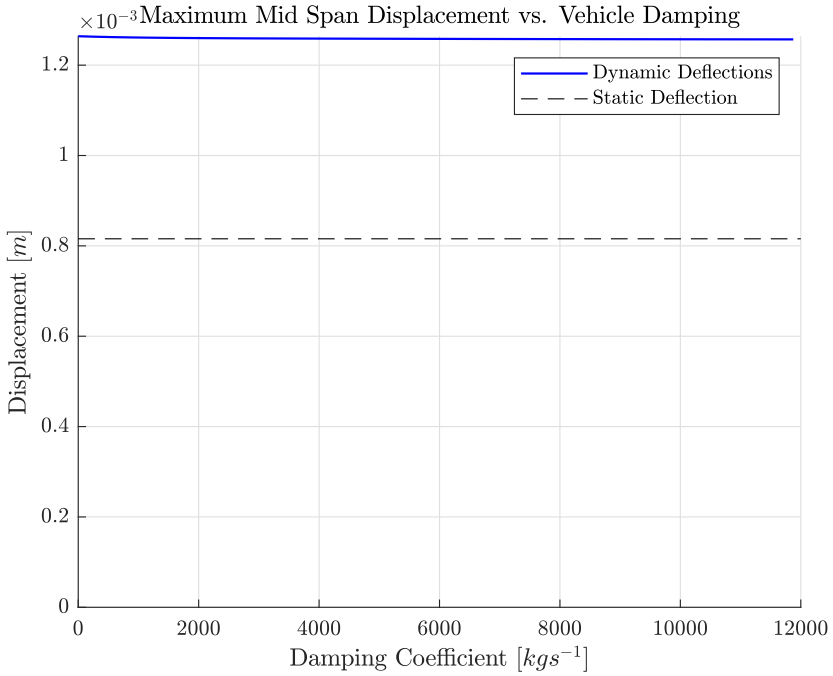

Figure 3.24: Maximum mid span deflections plotted against various secondary suspension damping rates.

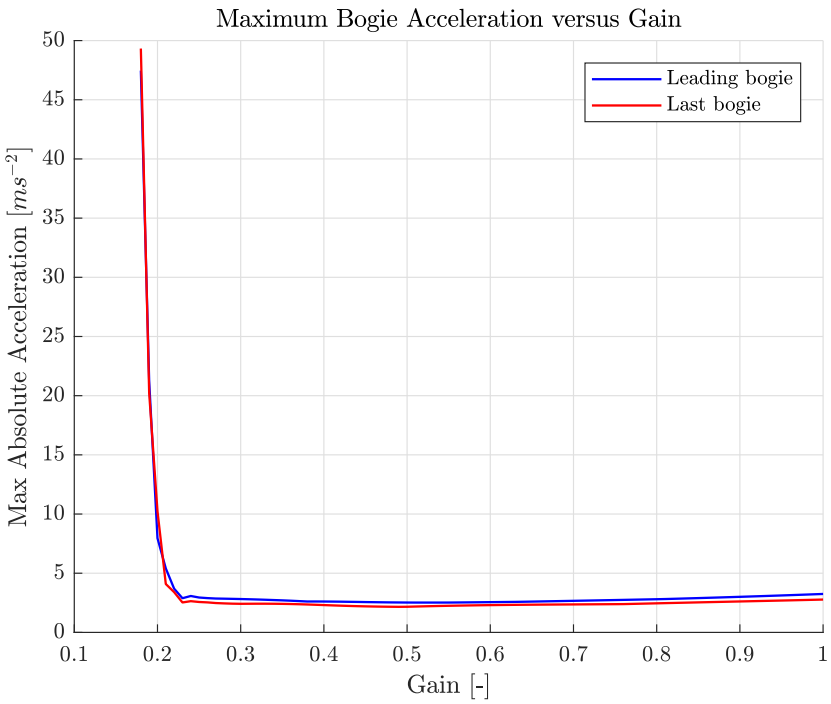

Figure 3.25: Maximum front and rear bogie acceleration for a range of multiples of the baseline controller gains.

3.1.7 Controller Gains

The gains of the controller have a direct effect on the way the vehicle responds to disturbances. Scaling the gains to higher values than those determined in section 2.6.3 would lead to instability. The system is unstable when the gains are smaller than 0.18× the baseline gains. The results of varying the gains from 0.18× to 1× their baseline values is shown in figures 3.25-3.27.

The results show that the effect of controller stiffness on the dynamic behaviour of the vehicle and the tube is fairly small for a wide range of gains, and that even for lower gains (up to 0.25× the baseline values), the effect of reducing the controller gains is negligible. After that point, the accelerations of the vehicle start rapidly rising. The mid span displacement also increases when the controller gains are reduced, but the overall effect is much smaller than the increase in accelerations of the vehicle.

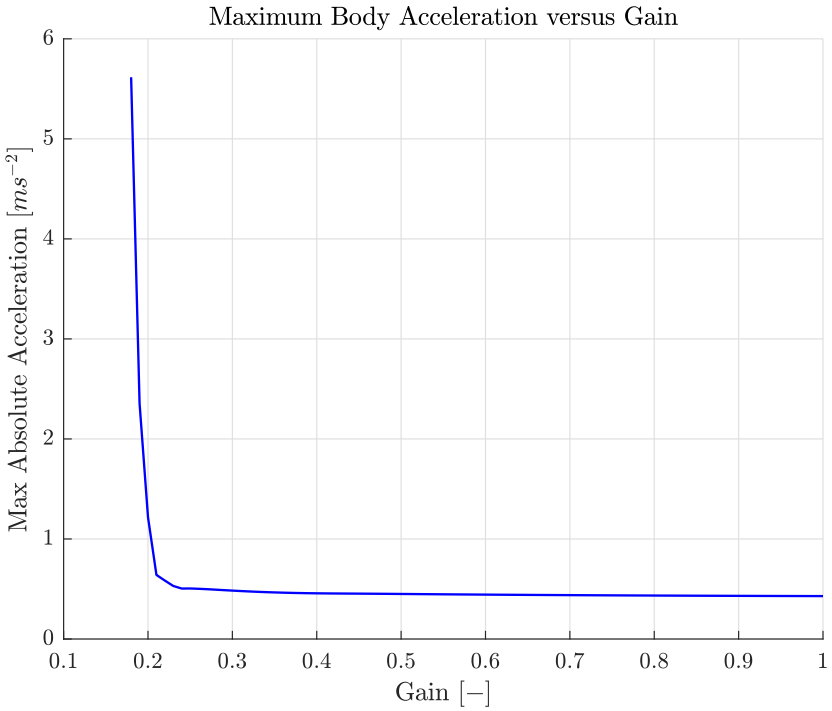

Figure 3.26: Maximum vehicle body acceleration for a range of multiples of the baseline controller gains.

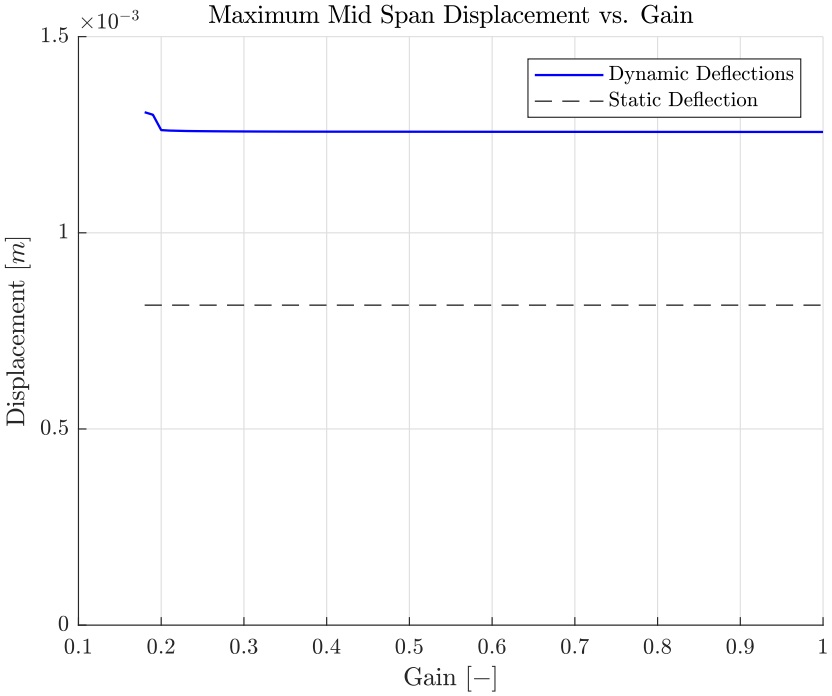

Figure 3.27: Maximum mid span displacement for a range of multiples of the baseline controller gains.

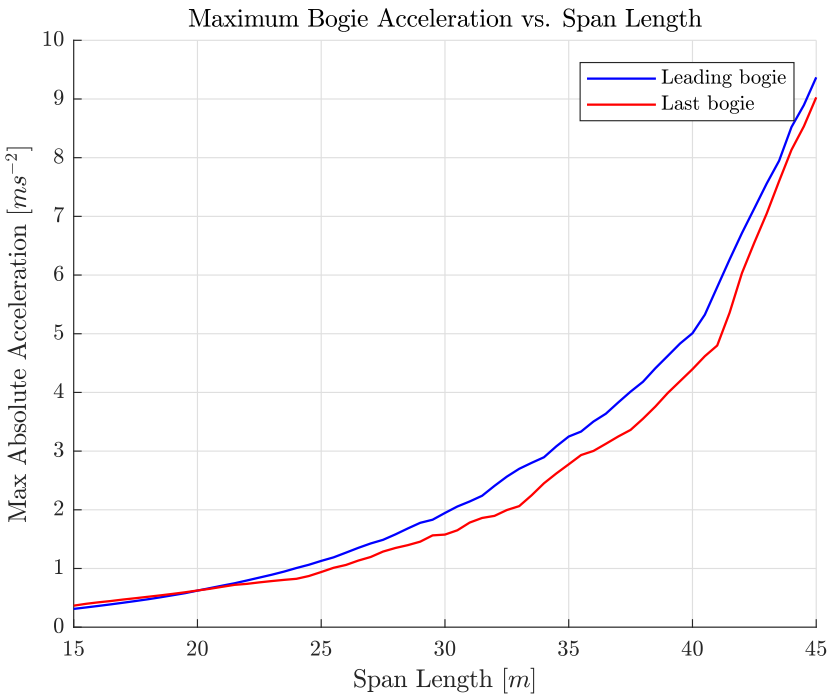

Figure 3.28: Maximum leading and last bogie accelerations for a range of guideway span lengths.

3.2 Effect of Varying Infrastructure Parameters

3.2.1 Support Spacing

Increasing the length of the tube spans will increase the deflections caused by an identical load. These increased deflections will also lead to increased accelerations on the vehicle body and bogies. Reducing the span length will require the placement of an increased number of supports along the route of the hyperloop, leading to an increase in costs. To strike a balance between comfort and cost, information is needed on the behaviour of the system for various span lengths. The results for are plotted in figure 3.28 - 3.30.

Increasing the span lengths leads to increasing accelerations and displacements. The displacements scale roughly by L^4, and the accelerations follow the upwards trend of the displacement. The difference between the static deflections and the dynamic deflections grow rapidly as the span length increases.

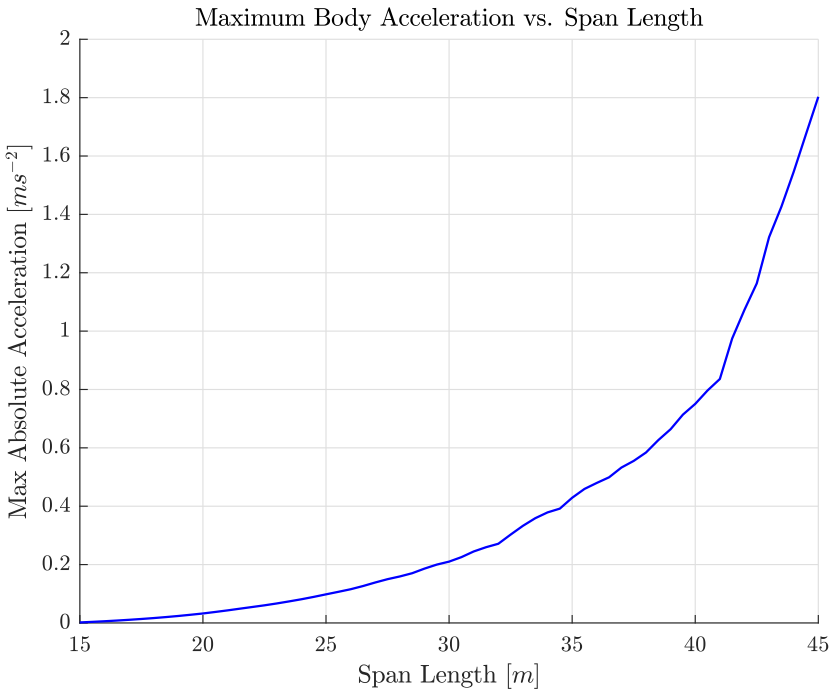

Figure 3.29: Maximum vehicle body accelerations for a range of guideway span lengths.

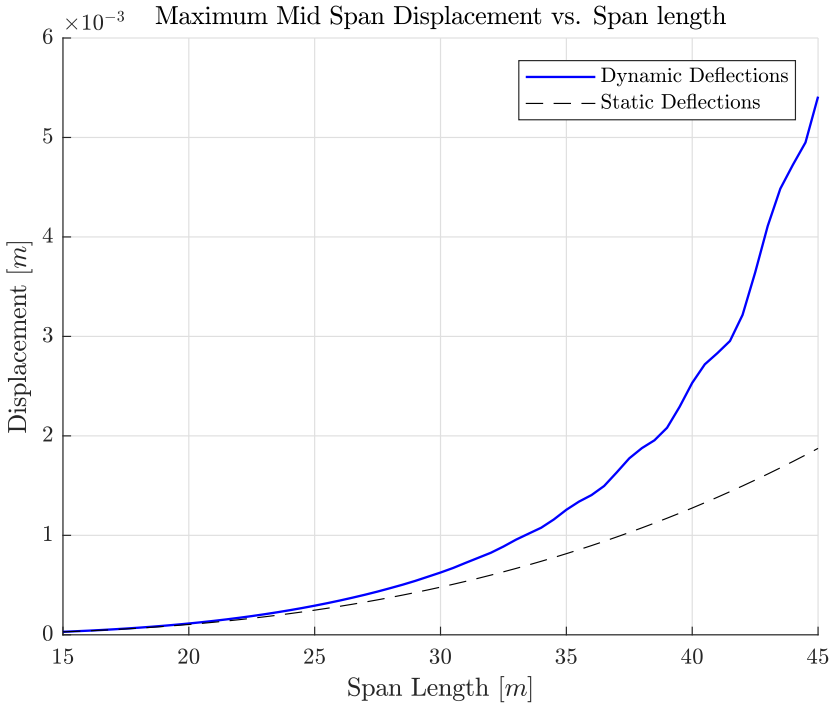

Figure 3.30: Maximum mid span displacements for a range of guideway span lengths, both static and dynamic results.

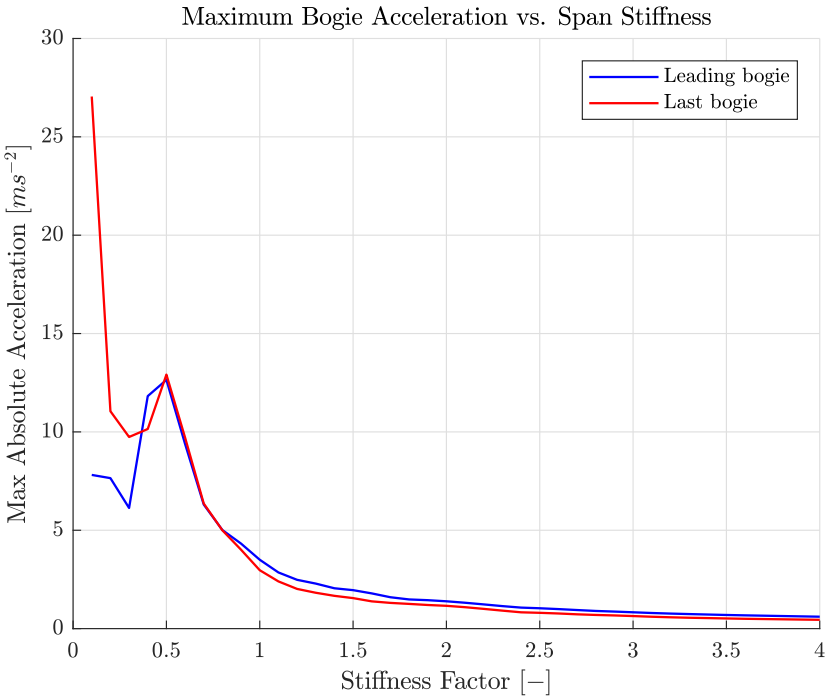

Figure 3.31: Maximum leading and last bogie accelerations for a range of guideway stiffness.

3.2.2 Guideway Stiffness

The stiffness of the tube has a major influence on the dynamic behaviour of the vehicle, as the additional deflections of the tube will directly lead to increases in accelerations of the vehicle. The effect of the track stiffness has been investigated over a range from 0.1× to 4× the baseline tube stiffness. The results are plotted in figures 3.31-3.33.

The general trend that is observed for midspan displacement, as well as body and bogie accelerations, is an inverse relationship of the form $\frac{1}{x}$. There is a large peak breaking this trend at 0.5× the baseline stiffness. The general trend as well as the observed peak will be further discussed in section 4.3.2.

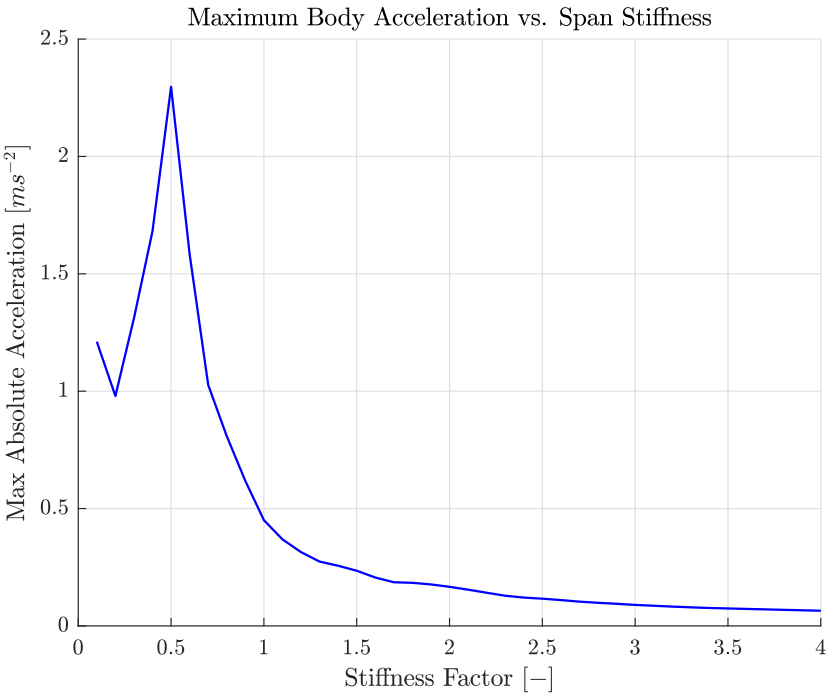

Figure 3.32: Maximum vehicle body acceleration for a range of guideway stiffness.

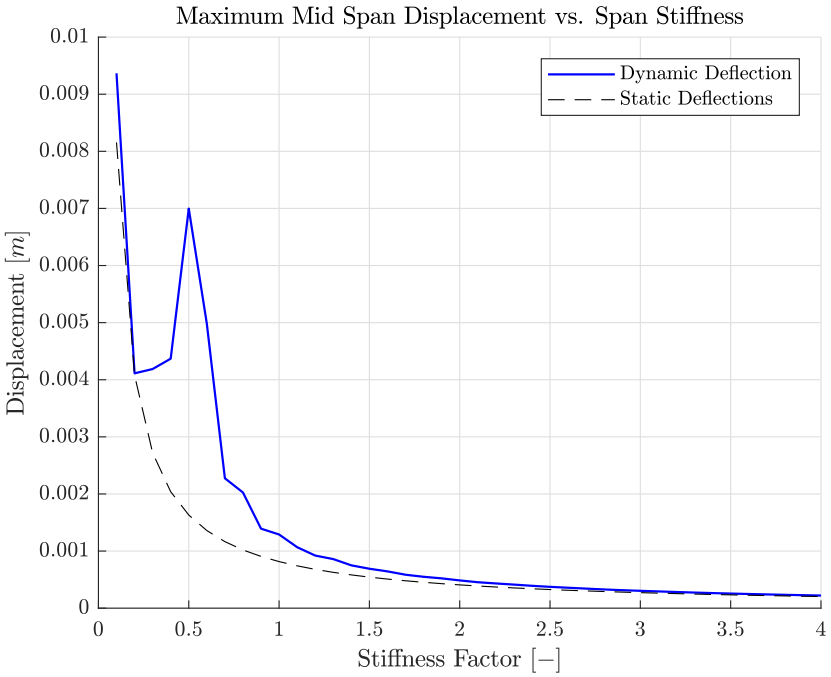

Figure 3.33: Maximum mid span displacements for a range of guideway stiffness, both static and dynamic results.

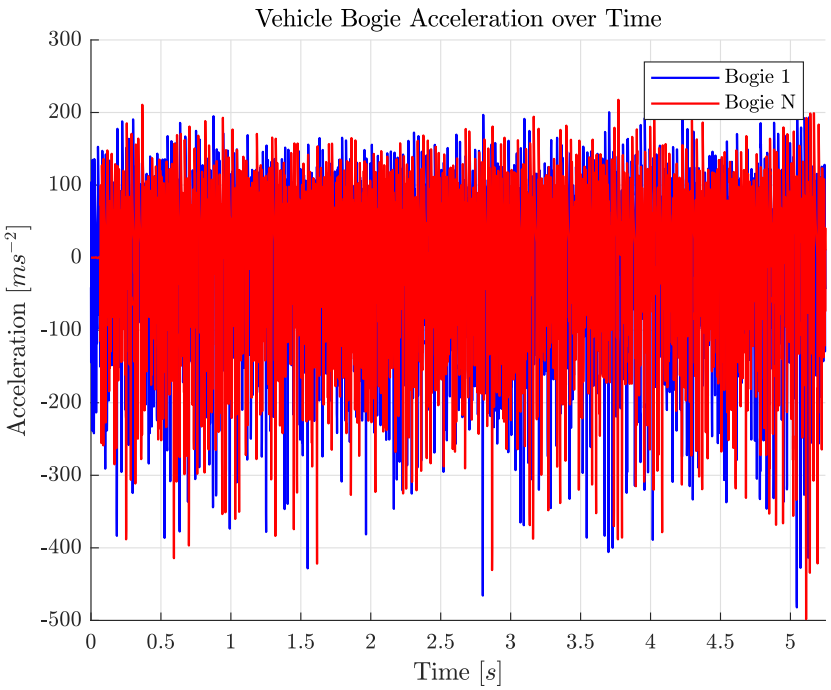

Figure 3.34: Baseline vehicle front and rear bogie acceleration over time including effects of track disturbance.

3.2.3 Guideway Imperfections

So far all results have been generated with the vehicle running on a perfectly smooth track, only disturbed from its equilibrium by the deflection of the tube. In reality, the vehicle will run on an imperfect track. A profile of such a track has been generated in section 2.5. The simulation results of the baseline vehicle running on the imperfect guideway are shown in figures 3.34-3.39.

A massive increase in bogie acceleration can be observed in figure 3.34. The bogies experience well over two orders of magnitude higher accelerations when running over an imperfect track surface. Spikes in acceleration of over $400ms^{-2}$ can be observed.

The body acceleration (figure 3.35) is heavily increased compared to the run on a perfect surface. The spikes in acceleration of around $1ms^{-2}$ are a common occurrence, which is $3\times$ higher than the peaks observed for the vehicle running on a perfect track surface(figure 3.2).

The maximum mid span displacement does not significantly increase due to the presence of guideway imperfections, with a maximum of $1.244mm$ compared to the $1.237mm$ of the undisturbed guideway.

The vehicle pitch angle attains significantly larger values when running over an imperfect surface, but in an absolute sense are still very low.

The magnet force varies a lot over time to deal with the track imperfections. While running over a perfect track, the force fluctuates around 1.04×10^4N (the static load a single axle would carry), with an amplitude of around 0.05×10^4N. When reacting to the track imperfections, the magnet force fluctuates much more significantly, with peaks of almost $7\times$ the static load,

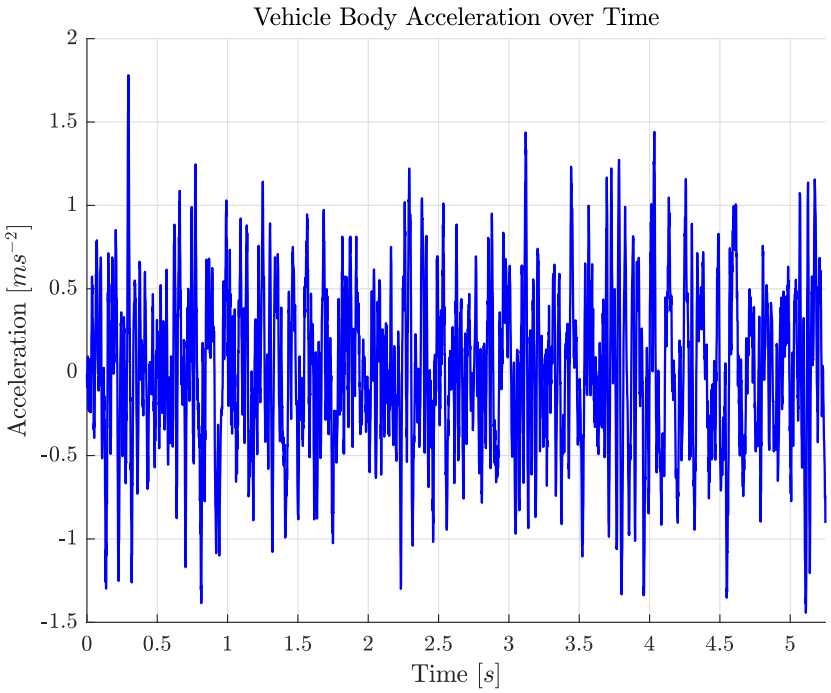

Figure 3.35: Baseline vehicle body acceleration over time including effects of track disturbance.

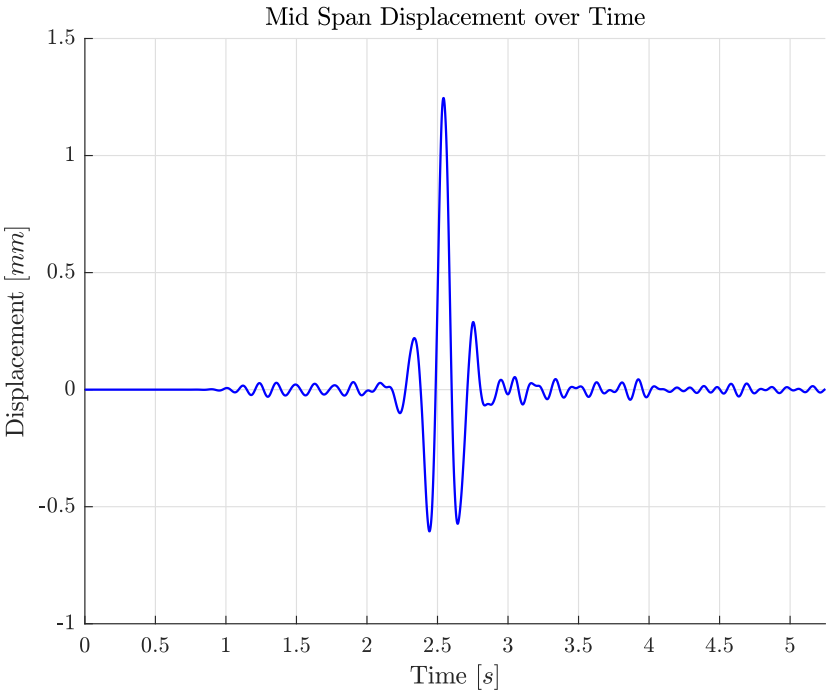

Figure 3.36: Baseline vehicle midspan displacement of tube over time including effects of track disturbance.

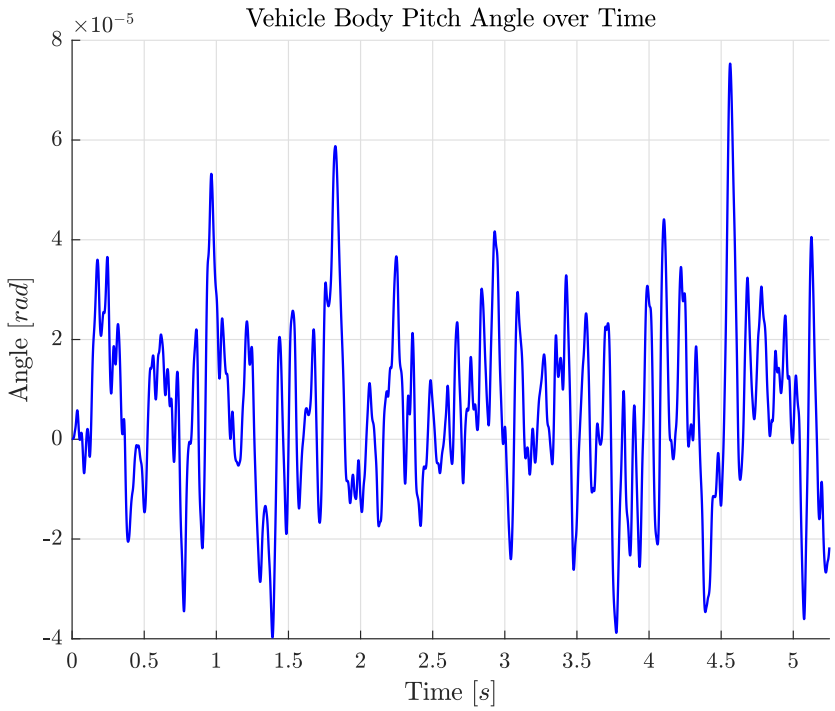

Figure 3.37: Baseline vehicle body pitch angle over time including effects of track disturbance.

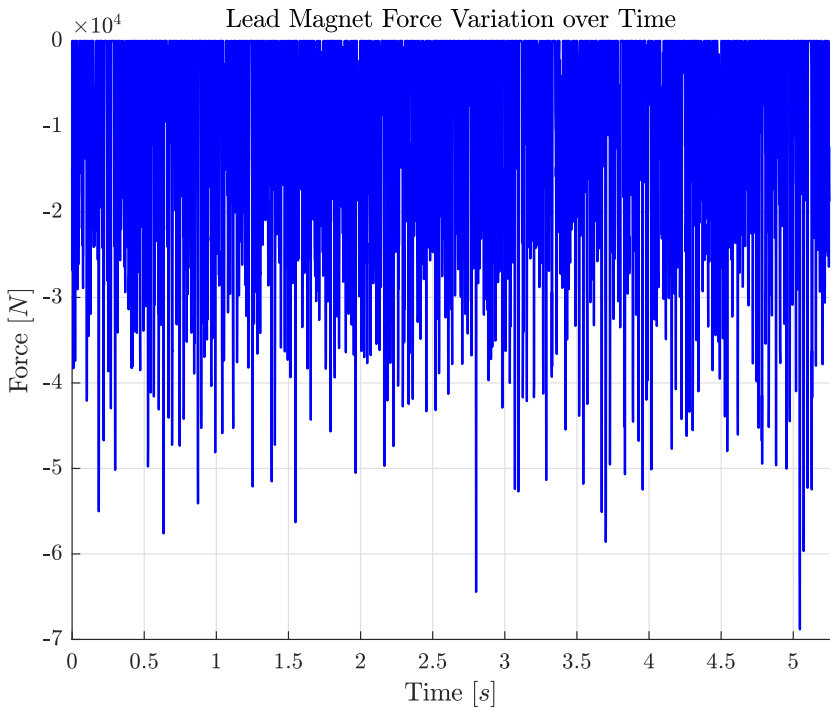

Figure 3.38: Lead magnet force variation over time for baseline vehicle including effects of track disturbance.

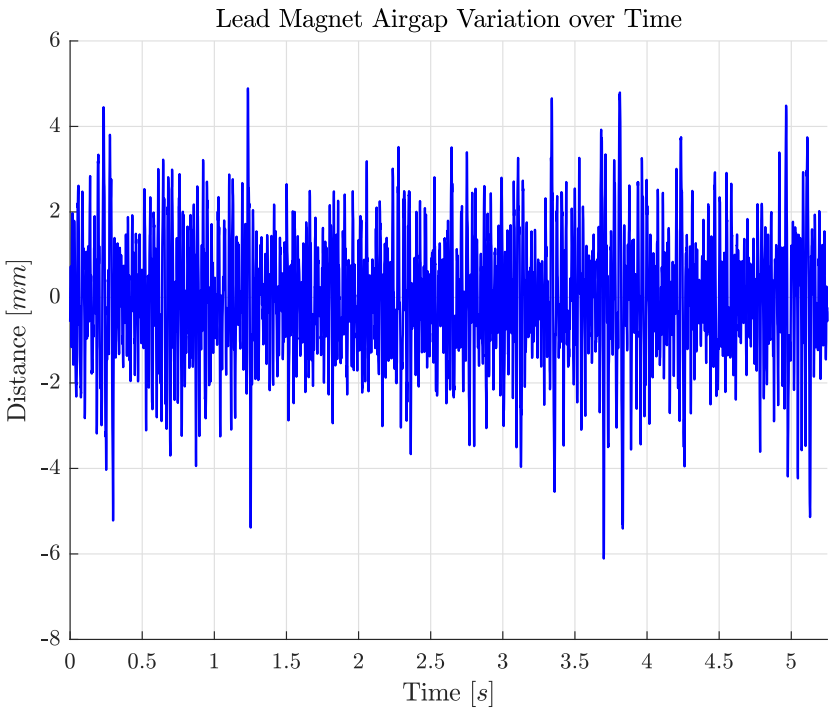

Figure 3.39: Baseline vehicle airgap variation of lead magnet including effects of track disturbance.

as well as moments of 0 force when the magnet would be required to push rather than pull to maintain a steady airgap.

The airgap variation of the magnets also drastically increases, with variations of up to $6mm$ from the set point of the controller, around $200\times$ the variation seen running over the flat track.

Chapter 4

Discussion

This chapter will discuss the trends shown in the data based on the results presented in chapter 3.

4.1 Baseline vehicle

Starting with the baseline vehicle and looking at the time-domain responses presented in chapter 3 (figures 3.1 - 3.3), one can observe higher frequency components in the response beyond the vibration period associated with the crossing time of the vehicle. By taking the Fourier transform of the time domain response the frequency spectrum of the response can be reproduced [35]. The spectra of the bogie acceleration, body acceleration and the displacement of the mid span are shown in figures 4.1 - 4.3.

Looking at the frequency domain for the response of the bogies in figure 4.1, the strongest peak can be observed at $8.54Hz$, the crossing frequency of the vehicle. Another small peak can be observed at $10.36Hz$, and the remainder of the peaks occur at integer multiples of the main $8.54Hz$ peak. A very similar pattern can be seen in figure 4.2 for the response of the vehicle body, with one notable exceptions: The peaks at the higher multiples of the crossing frequencies are almost completely damped out of the response by the secondary suspension. A small peak around $1.8Hz$ can also be observed, which is the heave motion of the vehicle.

Looking at the frequency response of the tube displacement in figure 4.3, the largest peak of the spectrum occurs around $4.5Hz$. When looking at the time domain response in figure 3.3, the vibrations induced by the vehicle passing the span have roughly this frequency, and indeed this peak is completely missing from the spectrum when the Fourier transform of the free vibration is taken from $t = 4s$ onwards (the red line in figure 4.3). The peaks in this free vibration spectrum are at $6.57Hz$, which is the first natural frequency of the tube, and at $10.36Hz$.

The increase in accelerations, forces, pitch angles and airgap variations observed at the end of the domain can be explained by the boundary condition at the end of the simulated section

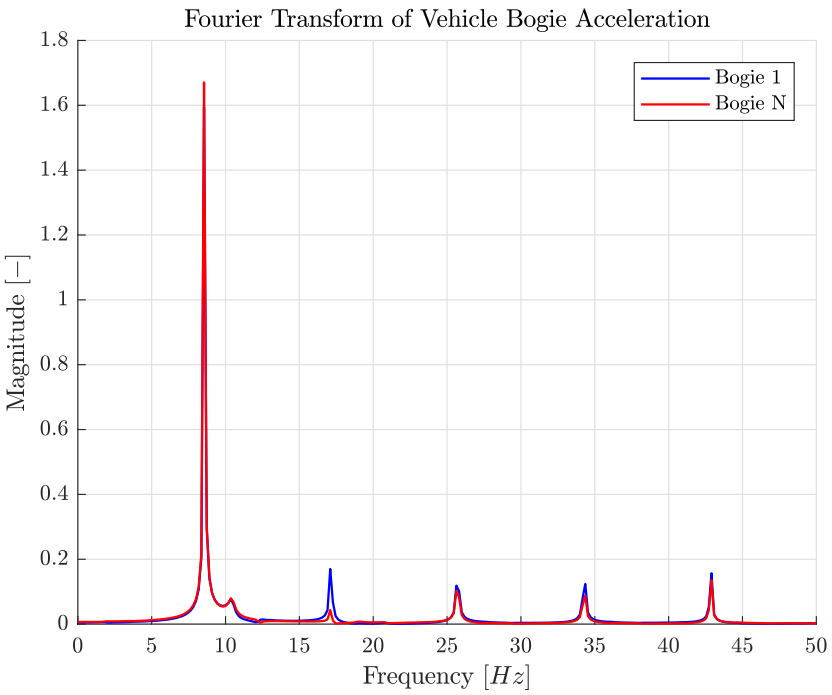

Figure 4.1: Frequency spectrum of front and rear bogie acceleration for the baseline vehicle.

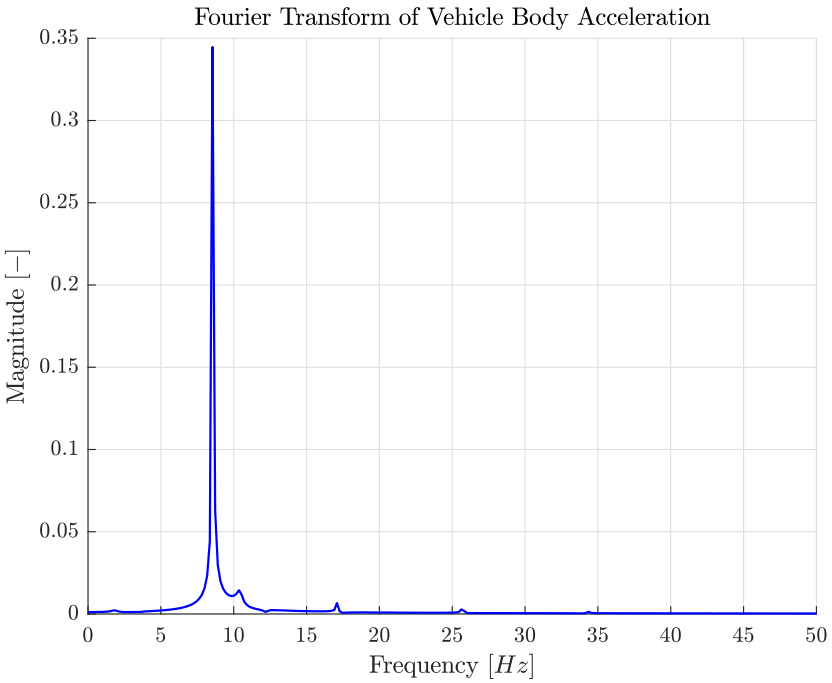

Figure 4.2: Frequency spectrum of vehicle body acceleration for the baseline vehicle.

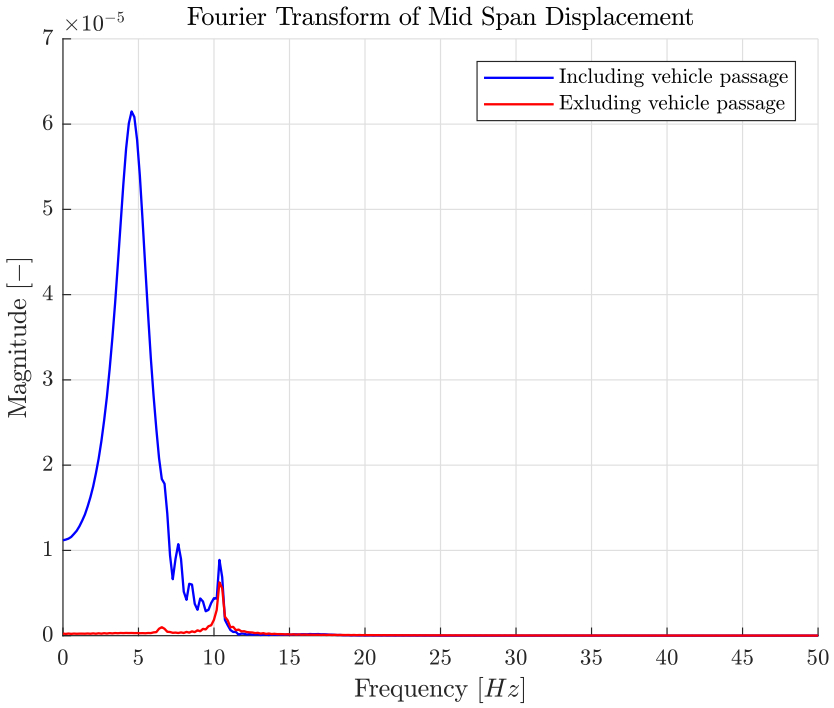

Figure 4.3: Frequency spectra of mid span displacement for the baseline vehicle. Blue spectrum is of the full time signal as in figure 3.3, red spectrum is the free vibration response of the beam from $t = 4s$ onwards.

of tube. As the vehicle reaches the end of the domain, the deflection of the tube increases since one end of the tube is now completely free to rotate rather than constrained by the next section of tube. This leads to the higher accelerations, forces, pitch angles and airgap variations seen in figures 3.1, 3.2 and **??**- 3.6.

4.2 Vehicle Parameters

4.2.1 Vehicle Speed

As the speed of the vehicle increases, the accelerations of the vehicle and the mid span displacement of the tube increase. These increases can be attributed to an increase in inertial load acting on the vehicle, caused by travelling along a curved path (the deflected tube) at increasing velocities. These effects are in line with the findings of Cifuentes, who attributes them to an increase in the centripetal and Coriolis force at higher velocities [11].

4.2.2 Vehicle Mass

The influence of vehicle mass on the dynamics behaviour of the vehicle, as outlined in section 3.1.2, is a linear increase in both accelerations and mid span displacement. The cause of the increase in displacement of the midspan is fairly straightforward, with the heavier vehicle leading to larger deflections. This also leads to the increases in body and bogie accelerations,

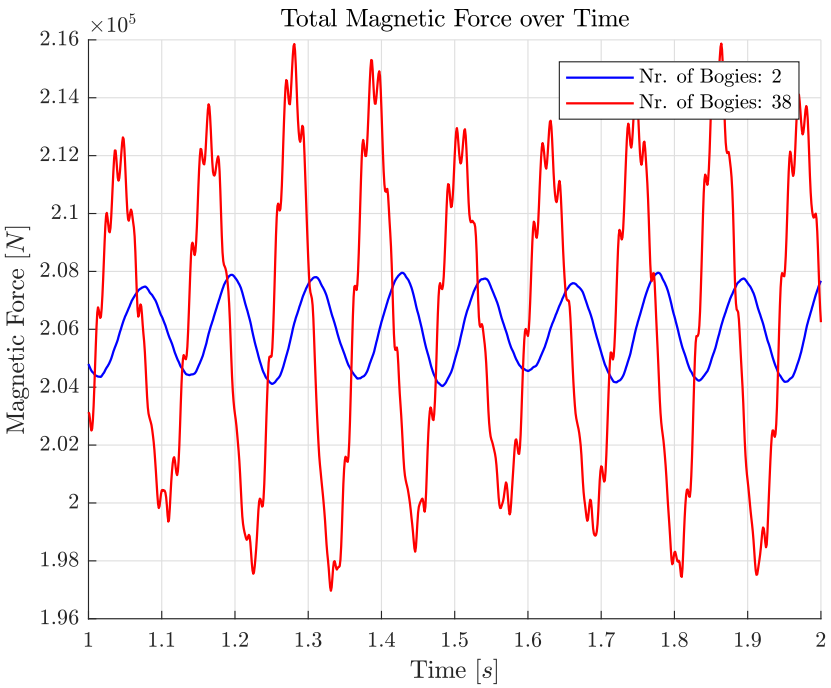

Figure 4.4: Total magnet force generated over a one second period for a 2 bogie vehicle and a 38 bogie vehicle.

which, as discussed in section 4.1 are driven primarily by the deflection of the tube as the vehicle traverses each span.

4.2.3 Number of Axles

An interesting results was highlighted in section 3.1.3, where the simulations indicate that an increasing number of axles would lead to an increase in the dynamic load on both the vehicle and the tube. Intuitively, one would expect that spreading the load out over a greater number of points would reduce the deflection of the tube, and by extension the accelerations of the pod body and bogies.

In contrast to these expectation, an increasing number of bogies leads to a sharp rise in tube displacements and vehicle accelerations. The cause of this behaviour lies in the loads generated in the magnets. Figure 4.4 shows the total magnet force generated to keep the bogies on their reference position for the vehicle with 2 bogies and the vehicle with 38 bogies over a period of one second. The 38 bogie vehicle shows much larger variations in the total force required for the control of the magnets than the 2 bogie vehicle.

A possible explanation for this behaviour lies in the fact that the controllers are completely independent of one another, while trying to make a line of magnets attached to a straight vehicle conform to a curved tube. This may lead to the controllers working against each other. This can visualized by thinking of a vehicle in the centre of a span. Assuming that the magnet at the centre of the vehicle is exactly at its set-point, the magnets at either end of the pod need to move closer to the tube to compensate, and will need to deliver a higher force to achieve this, which pulls the entire vehicle out of position and thereby triggers a

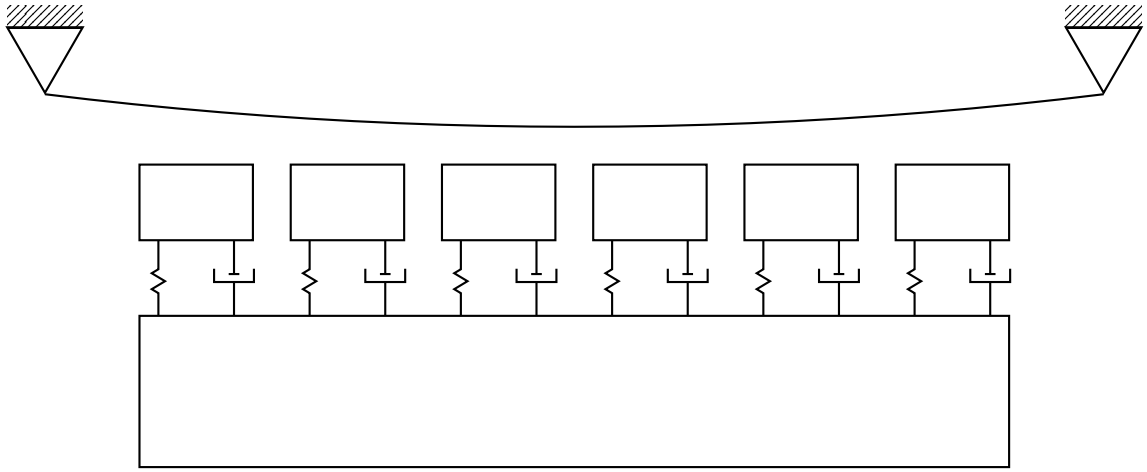

Figure 4.5: Schematic representation of a hyperloop vehicle on a displaced track. The outer bogies have to be pulled closer to the track surface to maintain their set point, while the inner bogies do not.

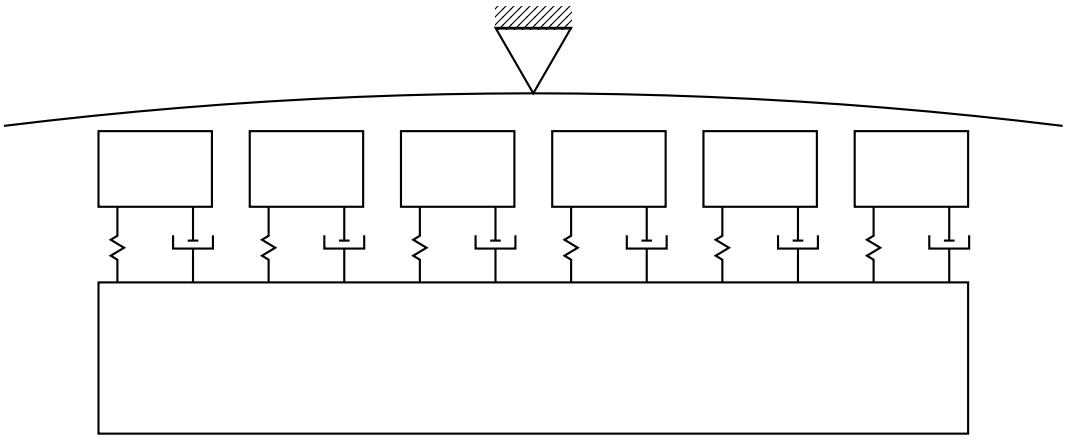

Figure 4.6: Schematic representation of a hyperloop vehicle on a displaced track. Shortly after the situation in figure 4.5, the vehicle crosses over a support. The situations shown in figure 4.6 is reversed, with the inner bogies having to be pulled closer tot the track to maintain their set point. This leads to the large fluctuations in magnetic force seen in figure 4.4.

force reduction at the centre magnet, which is now too close to the tube. As this occurs the pod also continues along the tube, and as the centre of the vehicle passes over a support, the situation reverses, with the outer magnets being forced closer to the tube and the centre magnet forced away from its set-point. The control systems then have to do the opposite from what they were doing before. The chosen control system tuning method, as described in section 2.6.3 leads to a system with a rapid rise time that is able to deal with these changes, at the cost of the overshoot observed in figure 4.4. The two situations outlined above are schematically represented in figures 4.5 and 4.6.

To overcome these problems, a control algorithm should be designed that accounts for the total state of the vehicle rather than one that only looks at the positions of the individual magnets.

4.2.4 Vehicle Length

Looking at figures 3.16-3.18, for vehicle from $20m - 35m$ long the trends in mid span displacement and accelerations are roughly linearly downward (for the lead bogie and the mid span displacement at least), corresponding to the load being more and more spread out over the tube span. When the vehicles are longer than 35m, the trend slows down and settles into a linear downward trend with a lower downward slope as the load is now spread out over two spans. The static displacement follows a similar pattern with increasing vehicle length, but with smaller changes in slope. At a vehicle length of around $55m$, the dynamic increase in mid span displacement is smallest, with a $1.12\times$ increase in maximum midspan displacement from the static to the dynamic case.

For the vehicle body, the behaviour is different. The linear decline until a length of 35m is followed, but at a length of 48m the acceleration of the body finds a local minimum before rising again to a local maximum at a length of 60m, followed by a linear decline in acceleration until a length of 70m. Without the dip around the 48m length, the overall trend graph looks similar to the trend observed for the lead bogie acceleration.

When looking at the frequency spectra of the lead bogie (figure 4.7) and the vehicle body (figure 4.8), it becomes clear that there is some sort of destructive interference going on in the vibration of the vehicle body. The bogie has a spectrum similar to the baseline spectrum for both the $48m$ vehicle and the $60m$ vehicle. However, the vehicle body of the 48m vehicle experiences significantly lower accelerations, stemming from a decrease in amplitude of the vibration at the crossing frequency. The cause for this destructive interference is not immediately clear and should be investigated in future work. By utilizing this cancellation mechanism, one could potentially increase the ride comfort of the vehicle by selecting an advantageous set of design parameters to ensure this cancellation effect occurs. For the longer vehicles modelled, it is likely the assumption of a rigid body vehicle breaks down. This should be investigated, and the effects of this change on the observed cancellation effect should also be determined.

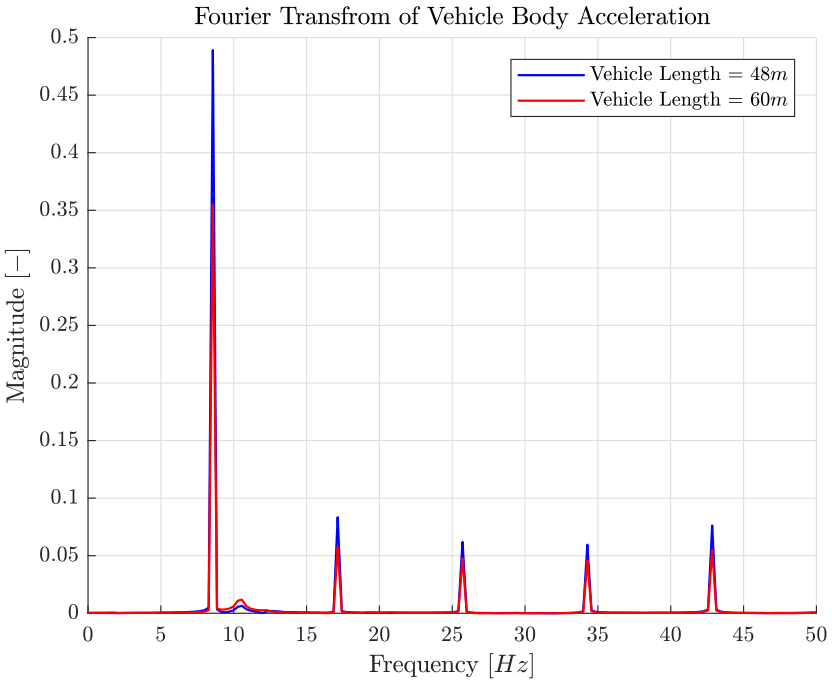

Figure 4.7: Comparison of frequency spectra for $48m$ and $60m$ vehicle lead bogie acceleration.

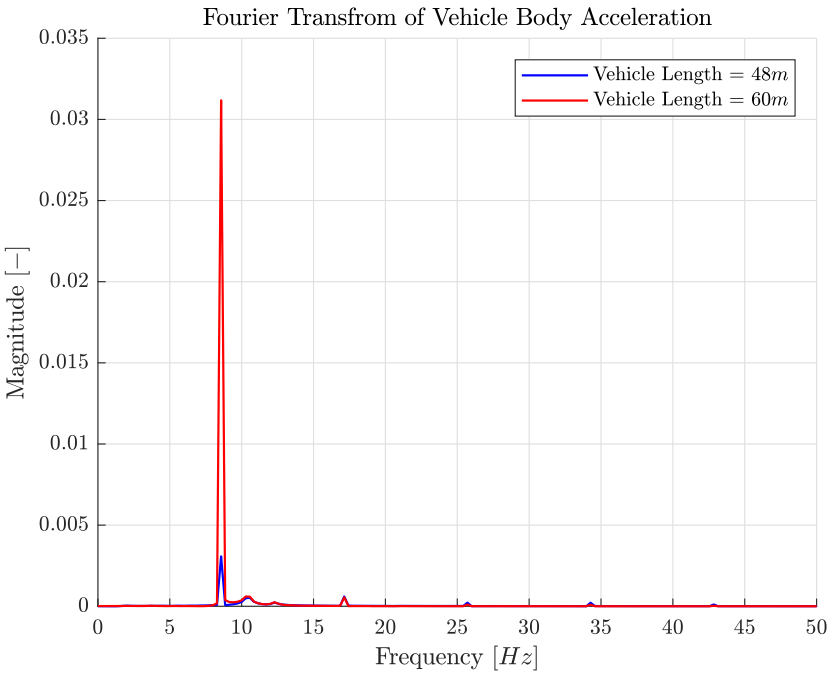

Figure 4.8: Comparison of frequency spectra for $48m$ and $60m$ vehicle body acceleration.

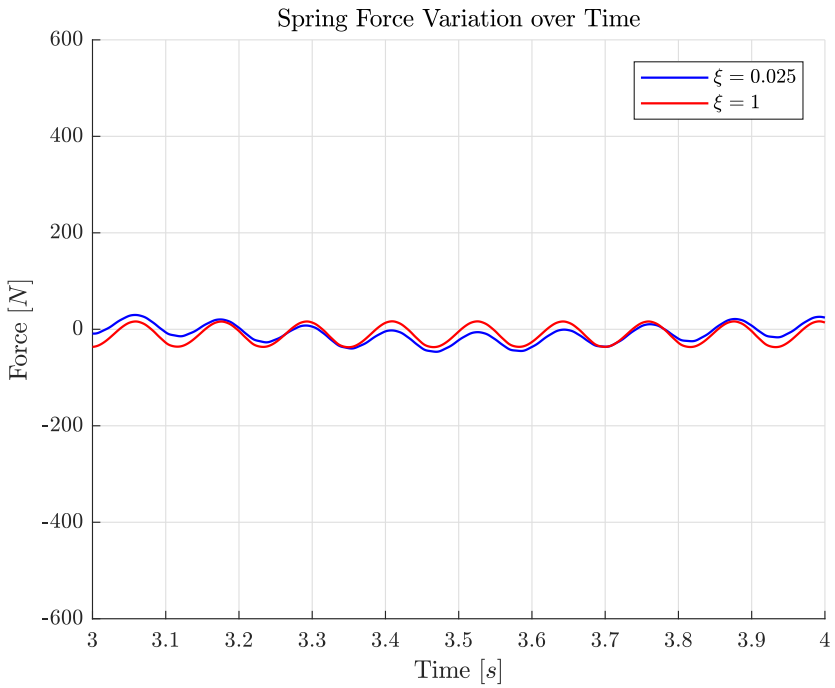

Figure 4.9: Variation of spring force from steady state load over a one second period for two damping ratios.

4.2.5 Vehicle Spring Rate

The dynamic behaviour of the vehicle is not heavily influenced by the changing of vehicle spring rates. Increasing the spring rate of the vehicle leads to slightly decreased bogie accelerations, and slightly increased body accelerations as observed in figures 3.19-3.21. It has virtually no effect on mid span displacements. The increase in body acceleration can be attributed to the fact that with higher spring stiffness, track disturbances are transferred more directly to the vehicle body. The increasing spring stiffness leads to reduced movement of the spring-damper system, limiting the ability of the damper to absorb energy.

4.2.6 Vehicle Damping

Based on the results in section 3.1.6, it is clear the critically damped vehicle is not an ideal solution, with significantly lower accelerations acting on the vehicle body when using much lower damping rates. As is illustrated in figures 4.9 and 4.10, the damping force is an order of magnitude larger than the spring force when $\xi = 1$, but of the same order of magnitude when $\xi = 0.025$. The critically damped secondary suspension is therefore far too viscous to allow it to properly reduce the accelerations experienced by the vehicle body. With this in mind,it may be wise for future studies to revisit the effect of spring stiffness on the dynamics of the hyperloop, since the dominance of damper forces in the system may have overshadowed the effects of changing the spring stiffness.

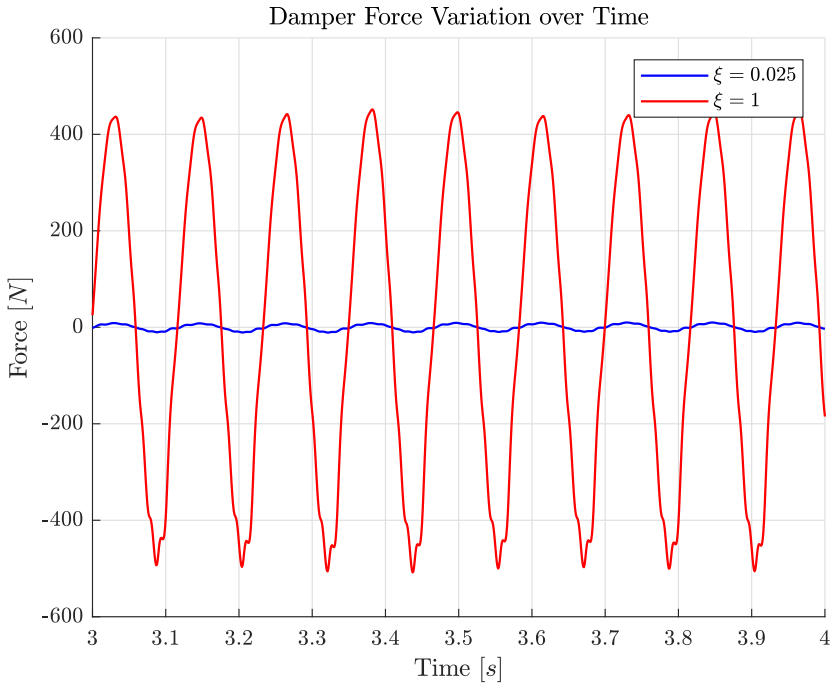

Figure 4.10: Variation of damper force over a one second period for two damping ratios.

4.2.7 Control System Gains

The results displayed in figures 3.25-3.27 show that for the stable range of gains from around 0.25× the baseline gains to the full baseline gains, the effect of varying the gains is very limited. The lower gains are sufficient to keep the bogies close to the set point of the controller with very little change in accelerations no change in mid span displacement. Below 0.25× the baseline gains, the accelerations start to increase exponentially as the gain is decreased towards the limit of 0.18× where the system becomes unstable. Although this study of the control system gains is quite limited in scope, it points to the importance of the controller, with dramatic increases in accelerations experienced by the vehicle if the controller is insufficiently stiff.

4.3 Infrastructure parameters

4.3.1 Support Spacing

Increasing the support spacing leads to increasing displacements and accelerations as shown in figures 3.28-3.30. The dynamic maximum guideway displacements increase at a much higher rate than the static maximum guideway displacements. A possible explanation for this behaviour is that the inertial loading that can be attributed to the vehicle travelling along a curved path is increased. This increase stems from an increase in path length and an increase in the curvature of the path due to the higher deflections that already follow from the increase in the overall span length. This then leads to higher centripetal and Coriolis forces.

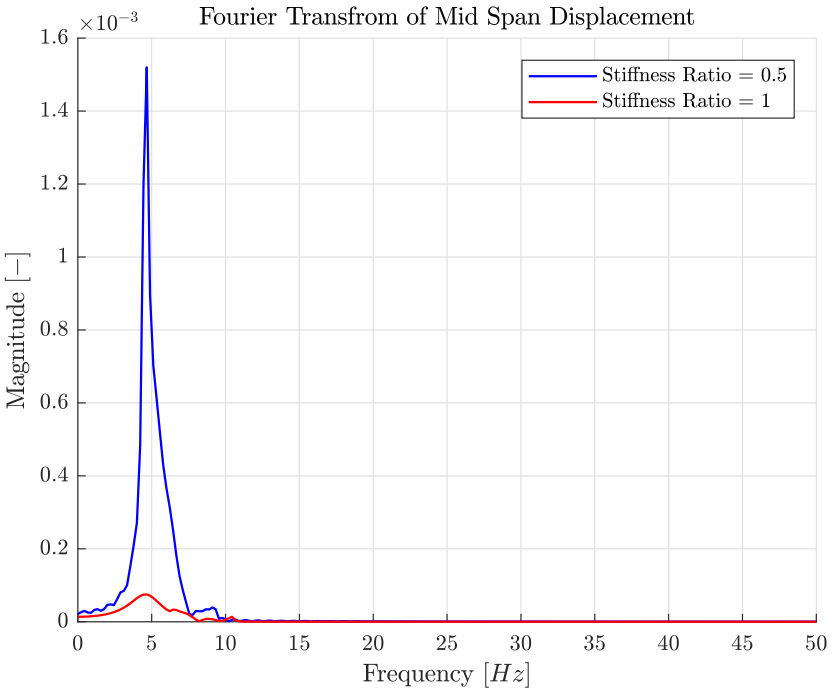

Figure 4.11: Frequency spectra of mid span displacements for stiffness ratios of $0.5 \times EI_{baseline}$ and $1 \times EI_{baseline}$.

4.3.2 Guideway Stiffness

Looking again at the figures produced in section 3.2.2 (figures 3.31-3.33), the overall trend that can be seen in the results is that the mid span displacements and the vehicle accelerations scale by some function of the form $^1/_x$, which is to be expected when realizing that the displacement equations of beams scale by $^1/_{EI}$. The same overall trend can be observed in figure 3.33 for the static deflections of the guideway.

The peak in the graph that breaks the general trend, around a stiffness ratio of 0.5× the baseline stiffness, can be explained by a resonance response of the tube. When the stiffness ratio equals 0.5, the first eigen frequency of the guideway is $4.56Hz$. This is very close to the frequency of the vibration introduced in the guideway by a crossing vehicle, which was around $4.5Hz$ as shown in section 4.1 and figure 4.3. This resonant loading leads to greatly increased mid span deflections and by extension higher vehicle accelerations. The frequency response spectra of the mid span displacement and vehicle body acceleration are shown in figures 4.11 and 4.12 for stiffness ratios of $0.5 \times EI_{baseline}$ and $1 \times EI_{baseline}$.

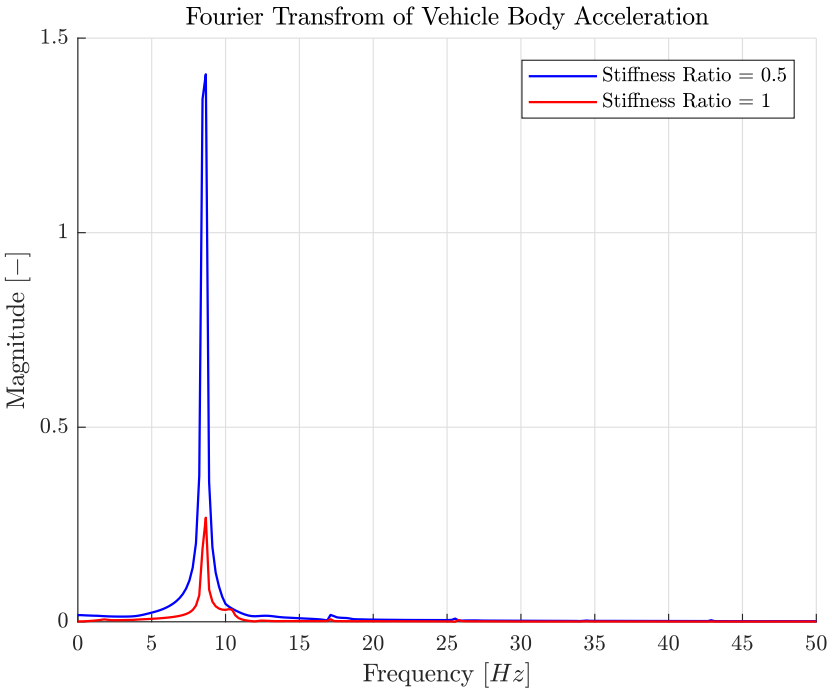

Figure 4.12: Frequency spectra of vehicle body acceleration for stiffness ratios of $0.5 \times EI_{baseline}$ and $1 \times EI_{baseline}$.

4.3.3 Guideway Imperfections

Looking at the results in section 3.2.3, it is clear that the introduction of guideway imperfections has a very significant impact on the overall performance of the vehicle, but a negligible impact on the dynamic displacement of the tube. This is in line with results obtained by Ren [36], who also noted the same trend.

The bogie and body accelerations are significantly higher, and have a significant high frequency component due to the added imperfections of the guideway surface. Looking at the Fourier transform of the bogie accelerations in figure 4.13, it is clear the bogie motions are completely dominated by the higher frequency components introduced by the imperfections in the guideway profile. This is especially obvious when contrasting the spectrum to the spectra of the undisturbed vehicle bogie accelerations in figure 4.1, which is comprised of the crossing frequency and its integer multiples.

The frequency response spectrum of the vehicle body is shown in figure 4.14. The body accelerations do not show this dominance of the higher frequency components, and the highest amplitude frequency component is still generated at the crossing frequency of the vehicle, implying that the deflection of the tube is still a significant contribution to the overall acceleration of the vehicle body. It also shows that the passive secondary suspension is capable of significantly reducing the effect of external disturbances acting on the vehicle body and by extension the passengers riding in the vehicle. Since the vehicle body motion due to guideway deflections is a significant part of the total vehicle body motion, it cannot be neglected in future work on the control system design.

The difference between the setpoint of the controller and the actual relative position of the

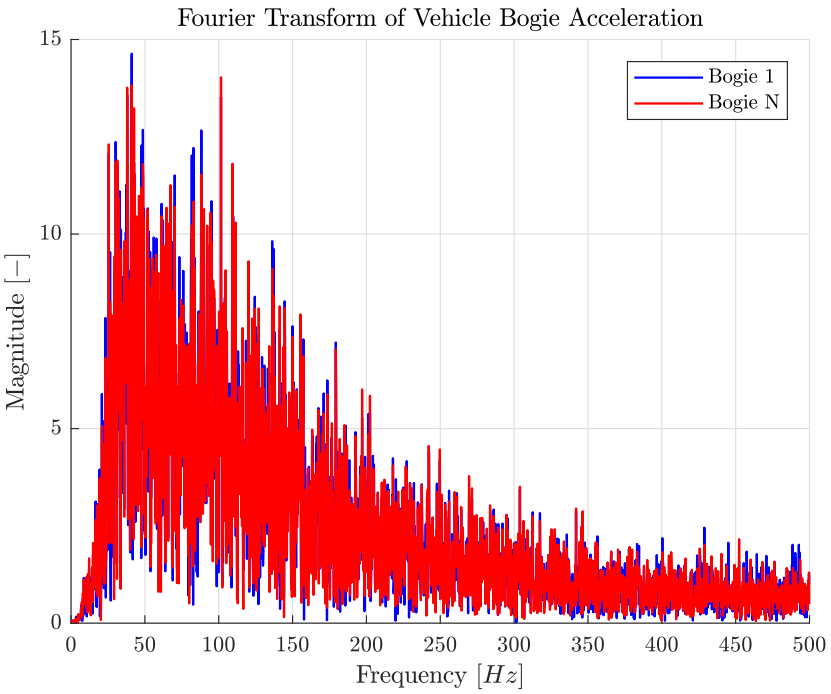

Figure 4.13: Frequency spectrum of lead and last vehicle bogies for the baseline vehicle running over an irregular guideway.

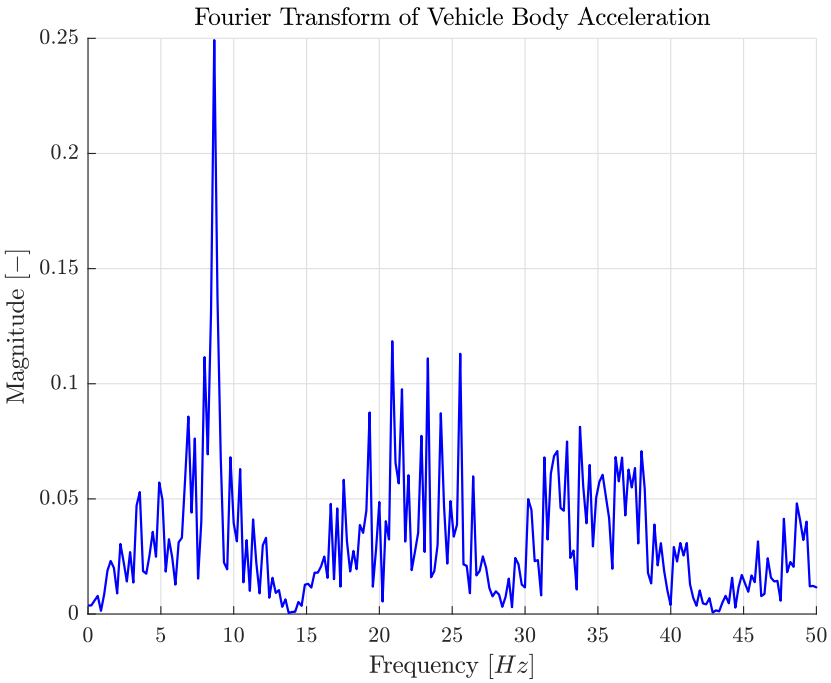

Figure 4.14: Frequency spectrum of the vehicle body for the baseline vehicle running over an irregular guideway.

Gain	value
K_p	$17.225 \cdot 10^6$
K_i	$5.2131 \cdot 10^7$
K_d	$4.8496 \cdot 10^5$

Table 4.1: New vehicle controller gains for reduced overshoot and slower rise time.

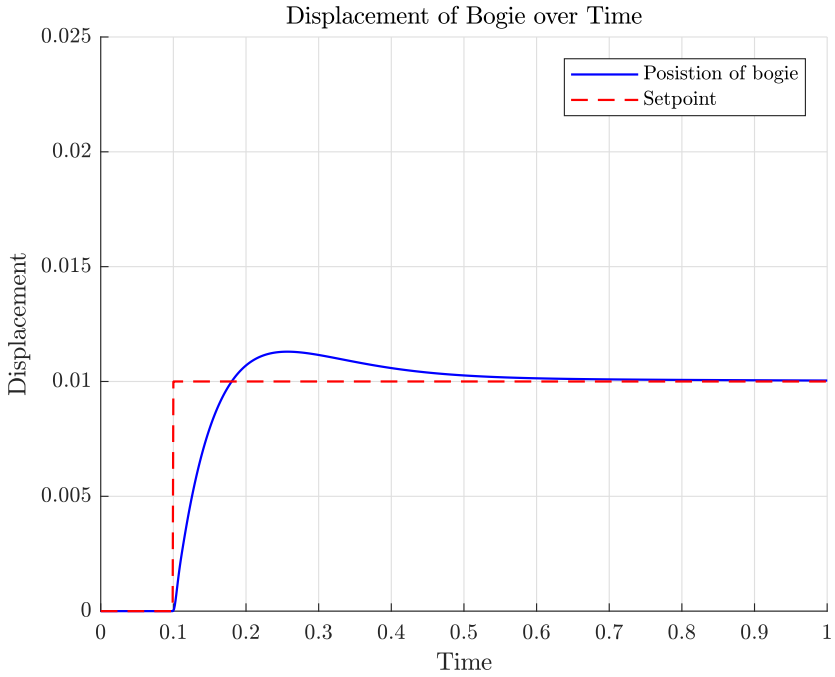

Figure 4.15: Step response of baseline vehicle bogie using new controller gains.

first bogie, shown in figure 3.39, varies significantly over time, with spikes up to $6mm$ seen over the course of the simulation. These large spikes can partly be attributed to the very stiff controller with large amounts of overshoot that was used in the study, and the rapid response of the vehicle to guideway disturbances leads to the high bogie and vehicle body accelerations.

Since the response of the controller used so appears to be too high to adequately deal with the track disturbances, a second set of PID gains has been generated, with the response manually tuned to have significantly lower overshoot and a slower rise time. The gains that were chosen for this updated controller are shown in table 4.1, and the step response of the controller is shown in figure 4.15. Using this controller to once again simulate the running of a baseline vehicle over the disturbance profile shown in figure 2.7, the accelerations of the vehicle bogies and body, and the airgap variation have been plotted in figures 4.16-4.18.

Contrasting figures 4.16-4.18 to figures 3.34, 3.35 and 3.39, it is clear that the accelerations acting on the bogies and body, as well as the airgap variations can be reduced significantly by appropriately tuning the control system. Despite this, the guideway imperfection still causes the accelerations experienced by the vehicle and the bogies to increase by an order of magnitude. Care must be taken in future designs to carefully tune the control system to minimize the influence of guideway disturbances, while at the same time steps must be taken to ensure that these disturbances are limited in the first place.

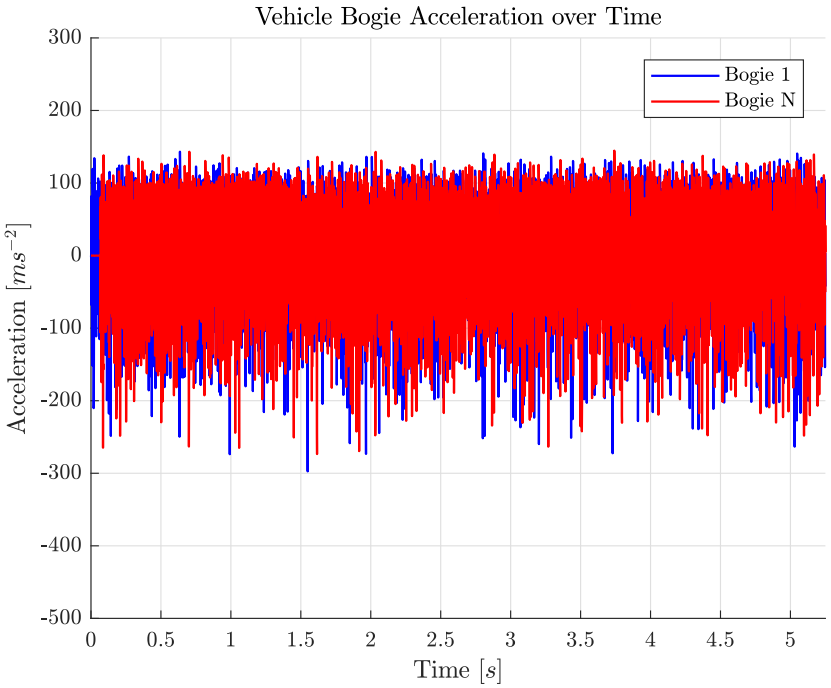

Figure 4.16: Baseline vehicle front and rear bogie acceleration over time including effects of track disturbance with new controller gains.

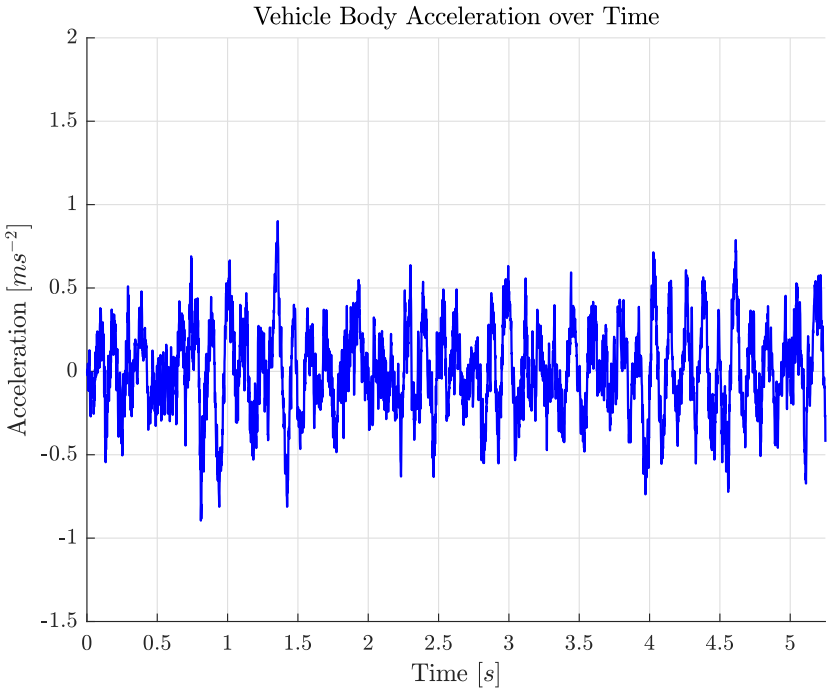

Figure 4.17: Baseline vehicle body acceleration over time including effects of track disturbance with new controller gains.

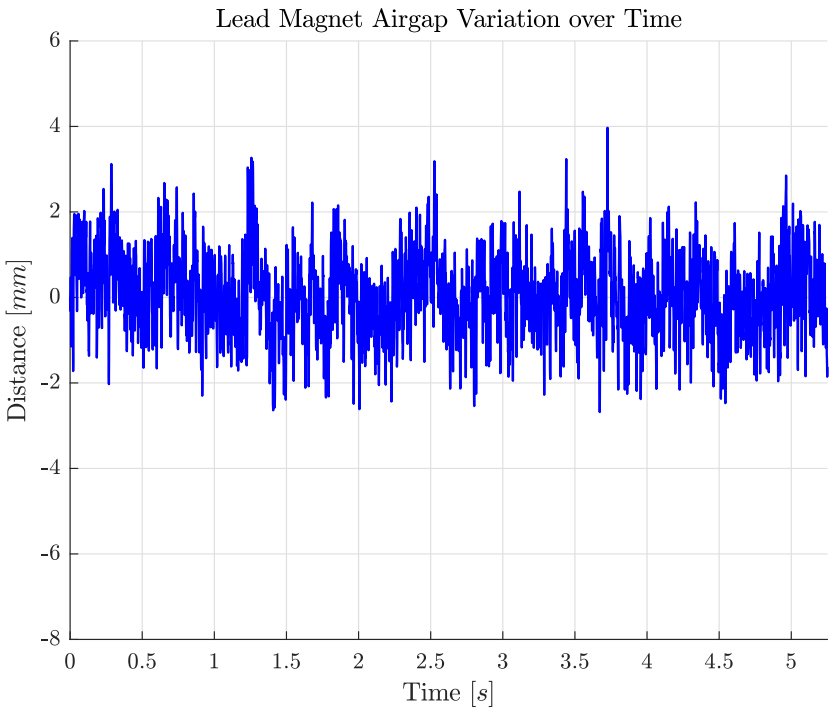

Figure 4.18: Baseline vehicle airgap variation of lead magnet including effects of track disturbance with new controller gains.

4.4 Future Outlook

In general, the baseline vehicle presented shows promising dynamic behaviour. The displacements of the tube are fairly small and the vehicle body accelerations are low. The pressurized tube provides sufficient stiffness for a 35m span length, although the deflections and accelerations increase rapidly for increasing span lengths. Decreasing the number of supports has the potential to dramatically reduce the implementation costs of a full scale system. From the results presented it is clear that if the span length is to be increased beyond $35m - 40m$, the stiffness of the spans has to be increased beyond that which is provided by the vacuum tube on its own. By combining the results presented in this study with a cost estimate of the tube and its supports, a well founded trade study can be made to select an appropriate span length and stiffness.

The model can be expanded to include lateral behaviour. The method for doing so would be practically identical to the method described here for the vertical dynamics. By modelling both vertical and lateral dynamics, the full range of motion passengers may experience can be predicted. This will allow a more complete assessment of the level of comfort the passengers will experience during various stages of a trip, such as straight line cruising, cornering and switching tracks.

The cancellation of the heave motion of the vehicle body observed in section 4.2.4 should be investigated further. Understanding this effect will allow one to design the system in such a way that this effect is exploited, which could for instance lead to a reduction in the number of supports the tube requires. In general, it would appear to be advantageous to use vehicles

that are longer than the span length of tubes. This has to be balanced with the increased mass of these longer vehicles. Assuming the mass of the vehicle scales roughly linearly with the vehicle length, and looking at figures 3.11 and 3.17, this would seem like a worthwhile trade off, since the decrease in body acceleration due to the increase in vehicle length is significantly higher than the increase in body acceleration due to vehicle mass. In the end, the vehicle length will not only be decided by dynamic considerations, but also the required capacity of the system and logistics in the stations.

As was demonstrated in section 4.3.3, properly tuning the control system has a large impact on the performance on the vehicle when an imperfect track surface is encountered. The design and the method for tuning the control system were, due to the scope of the study, fairly rudimentary. A more dedicated study into the control system could see further improvements in the dynamic behaviour of the vehicle. Any control system that predicts the magnetic force $F_m^{t+\Delta t}$ based on the vehicle and track state at a time t can be readily implemented into the presented model.

The design of the secondary suspension can be investigated in more detail. Properly choosing spring and damping rates will have a significant impact on the dynamic behaviour of the vehicle body. More complicated suspension mechanisms can also be modelled using the presented methodology. Common elements present on current rail vehicles such as air springs and velocity dependent dampers, which show non-linear behaviour dependant on displacement and/or velocity, can also be accounted for. In such a case, the solution procedure outlined in chapter 2 would have to include an iterative solution procedure for the vehicle response within each time step.

The guideway irregularity model should be verified against real world data of newly laid tracks. The model is based on the maximum allowed PSD for high speed rail in Germany, at which point rail maintenance would have to take place. This does mean that the model accounts for wear and tear from contact between the wheels of trains and the track. There is no contact between the guideway and the vehicle, and the used model may therefore simply be far too conservative in the its estimation of the irregularity that may be encountered.

In general, there do not appear to be any fundamental obstacles to running a hyperloop vehicle at $300ms^{-1}$ across a flexible guideway. The baseline vehicle performs adequately and, with several tweaks to the damping ratio, vehicle length and the control system gains, can be designed in such a way that a smooth ride for passengers can be ensured.

Chapter 5

Conclusion

The model presented has captured the dynamic behaviour of a hyperloop vehicle and guideway in such a way that both resonance and cancellation effects can be observed. It can be used as a rough design tool for estimating the overall effect that several key design parameters have on the behaviour of the system, and for the early identification of resonance issues that are to be avoided. Due to the lack of data that can be used to validate the model, the magnitudes of results such as acceleration data and guideway displacements should be treated with a degree of suspicion if they are to be used for future design work.

The vehicle simulated is fairly simplistic compared to vehicles that are currently in use in other forms of mass transit. More complicated vehicle models are readily accommodated by the method presented as long as mass, stiffness and damping matrices of similar form to the matrices derived in section 2.2 are created to represent the vehicle. For long vehicles the deformation of the vehicle body may be a significant factor in the overall vehicle motion. This could lead to further dynamic interactions while travelling along the guideway, and the influence of using a deformable body in place of a rigid body should be investigated.

The model is readily expanded to include lateral dynamics, which have been neglected so far. The fundamental way of constructing the model is the same when lateral dynamics are included, with an additional set of terms in the vehicle and guideway matrices to account for the lateral motions and potential the coupling of lateral and vertical dynamics. With the addition of lateral dynamics the complete behaviour of the vehicle can potentially be simulated.

As was noted several times in the discussion of the results, the PID control method used, while sufficient to answer the questions posed for this study, will not suffice for the actual vehicle. The development of a control system that can adequately deal with guideway imperfections while the vehicle travels at $300ms^{-1}$ will be important for the successfully implementation of the hyperloop system. Ideally, a controller would be developed that is capable of recognizing the difference between guideway displacements and guideway imperfections, thereby allowing the control system to reject the higher frequency components of the setpoint signal caused by the guideway imperfections. This would allow the vehicle to operate much more like it would

operate on a perfectly smooth guideway, and will allow a dramatic increase in ride comfort. Future work on the control system cannot neglect the effects of guideway displacements, as they form a significant part of the vehicle body motion.

Based on the results of the baseline vehicle, it is clear the secondary suspension is a necessary part of the vehicle. Vehicle body accelerations are reduced by an order of magnitude by the secondary suspension, and the higher frequencies in the vehicle bogie response are removed from the response spectrum. Especially when an imperfect guideway is considered, the secondary suspension is indispensable. Using the presented model, the performance of more complicated suspension setups can be evaluated to further increase passenger comfort.

The causes of resonance and cancellation should be investigated further. Once the mechanisms and their relation to vehicle and guideway parameters are better understood, the vehicle and guideway can be designed in such a way that the accelerations of the body or the deflections of the guideway are minimized. Reducing vehicle body accelerations would lead to a more comfortable ride for the passengers, while decreasing guideway deflections will limit the dynamics stress introduced by the passage of the pods.

References

[1] Yeong-Bin Yang and Jong-Dar Yau. Vehicle-Bridge Interaction Element for Dynamic Analysis. *Journal of Structural Engineering*, 123(11):1512–1518, nov 1997.

[2] Elon Musk. Hyperloop Alpha. Technical report, SPACE EXPLORATION TECHNOLOGIES CORP, Hawthorne, 2013.

[3] E. A. Hodgkinson. Report of the Commissioners Appointed to Enquire into the Application of Iron to Railway Structures. Technical report, Cambridge [England] :, 1849.

[4] SGG Stokes. Discussion of a differential equation relating to the breaking of railway bridges. 1849.

[5] S.P. Timoshenko. On the forced vibrations of bridges. *Philosophical Magazine*, pages 1018–1019, 1922.

[6] Ladislav Fryba. *Vibration of solids and structures under moving loads*. ThomasTelford, Prague, 3rd edition, 1972.

[7] F. V. Filho. Finite Element Analysis of Structures Under Moving Loads. *The Shock and Vibration Digest*, 10:27–35, 1978.

[8] M. Olsson. Finite element, modal co-ordinate analysis of structures subjected to moving loads. *Journal of Sound and Vibration*, 1985.

[9] D. M. Yoshida and W. Weaver. Finite-element analysis of beams and plates with moving loads. *International Association of Bridge and Structural Engineering*, 31(1):179–195, 1971.

[10] John E. Akin and Massood Mofid. Numerical Solution for Response of Beams with Moving Mass. *Journal of Structural Engineering*, 115(1):120–131, jan 1989.

[11] Arturo O. Cifuentes. Dynamic response of a beam excited by a moving mass. *Finite Elements in Analysis and Design*, 5(3):237–246, 1989.

[12] H. H. Richardson and D. N. Wormley. Transportation Vehicle/Beam-Elevated Guideway Dynamic Interactions: A State-of-the-Art Review. *Journal of Dynamic Systems, Measurement, and Control*, 96(2):169, 1974.

[13] J. E. Snyder and D. N. Wormley. Dynamic Interactions Between Vehicles and Elevated, Flexible Randomly Irregular Guideways. *Journal of Dynamic Systems, Measurement, and Control*, 99(1):23, 1977.

[14] Y. Cai, S.S. Chen, D.M. Rote, and H.T. Coffey. Vehicle/guideway Interaction For High Speed Vehicles On A Flexible Guideway. *Journal of Sound and Vibration*, 175(5):625–646, 1994.

[15] Shibo Ren. *Dynamic Simulation of the Maglev Guideway Design*. PhD thesis, Delft University of Technology, 2008.

[16] Yeong-Bin Yang and Jong-Dar Yau. Vehicle-Bridge Interaction Element for Dynamic Analysis. *Journal of Structural Engineering*, 123(11):1512–1518, nov 1997.

[17] Hossein Azimi, Khaled Galal, and Oscar A. Pekau. A modified numerical VBI element for vehicles with constant velocity including road irregularities. *Engineering Structures*, 33(7):2212–2220, 2011.

[18] M Moghaddas, R Sedaghati, E Esmailzadeh, and P Khosravi. Finite element analysis of a Timoshenko beam traversed by a moving vehicle. *Proceedings of the Institution of Mechanical Engineers, Part K: Journal of Multi-body Dynamics*, 223(3):231–243, sep 2009.

[19] E.S Hwang and A.S Nowak. Simulation of Dynamic Load for Bridges. *Journal of Structural Engineering*, 117(5):1413–1434, 1991.

[20] H. XIA, Y.L. XU, and T.H.T. CHAN. DYNAMIC INTERACTION OF LONG SUSPENSION BRIDGES WITH RUNNING TRAINS. *Journal of Sound and Vibration*, 237(2):263–280, oct 2000.

[21] Michal Majka and Michael Hartnett. Effects of speed, load and damping on the dynamic response of railway bridges and vehicles. 2007.

[22] Van Nguyen Dinh, Ki Du Kim, and Pennung Warnitchai. Dynamic analysis of three-dimensional bridge-high-speed train interactions using a wheel-rail contact model. *Engineering Structures*, 31(12):3090–3106, dec 2009.

[23] N.M. Newmark. A Method of Computation for Structural Dynamics, 1959.

[24] K. J. Bathe. *Finite Element Procedures*. K.J. Bathe, 2nd edition, 2014.

[25] Z Friedman and J B Kosmatka. AN IMPROVED TWO-NODE TIMOSHENKO BEAM FINITE ELEMENT. *Computers & Structures*, 47(3):473–481, 1993.

[26] Z. Friedman and J. B. Kosmatka. An improved two-node timoshenko beam finite element. *Computers and Structures*, 47(3):473–481, 1993.

[27] G. R. Cowper. The Shear Coefficient in Timoshenko's Beam Theory. *Journal of Applied Mechanics*, 33(2):335, jun 1966.

[28] Samuel Earnshaw. Transactions of the Cambridge Philosophical Society. *Rendiconti del Circolo Matematico di Palermo*, 7(1):64, 1893.

[29] N H Vrijsen, J W Jansen, John Compter, and E A Lomonova. Measurement method for determining the magnetic hysteresis effects of reluctance actuators by evaluation of the force and flux variation. *The Review of scientific instruments*, 84:75003, 2013.

[30] N. Minorsky. DIRECTIONAL STABILITY OF AUTOMATICALLY STEERED BODIES. *Journal of the American Society for Naval Engineers*, 34(2):280–309, mar 1922.

[31] Hitoshi Tsunashima and Masato Abe. Static and dynamic performance of permanent magnet suspension for maglev transport vehicle. *Vehicle System Dynamics*, 29(2):83–111, 1998.

[32] Hardt Global Mobility. Hardt Internal Documentation. Technical report, 2017.

[33] D. J. Inman. *Engineering vibration*. Prentice Hall, 2001.

[34] J. G. Ziegler and N. B. Nichols. Optimum settings for automatic controllers. *Transactions of the ASME*, 64(11), 1942.

[35] Rodger E Ziemer. Signals and Systems: Continuous and Discrete (4th Edition). *Publisher: Pearson*, 1998.

[36] Shibo Ren, Arie Romeijn, and Kees Klap. Dynamic Simulation of the Maglev Vehicle/Guideway System. *Journal of Bridge Engineering*, 15(3):269–278, 2010.